

1 Seismic imaging across fault systems in the Abitibi greenstone belt – 2 An analysis of pre- and post-stack migration approaches in the 3 Chibougamau area, Quebec, Canada

4
5 Saeid Cheraghi¹, Alireza Malehmir², Mostafa Naghizadeh¹, David Snyder¹, Lucie Mathieu³, Pierre
6 Bedeaux³

7
8 ¹ Mineral Exploration Research Centre, Harquail School of Earth Sciences, Goodman School of Mines, Laurentian
9 University, Sudbury, Ontario

10 ² Department of Earth Science, Uppsala University, Uppsala, Sweden

11 ³ Centre d'études sur les ressources minérales (CERM), Département des Sciences appliquées, Université du Québec à
12 Chicoutimi (UQAC), Chicoutimi, Québec

13 *Correspondence to:* Saeid Cheraghi (scheraghi@laurentian.ca)

14 **Abstract.** Two high-resolution seismic reflection profiles acquired north and south of Chibougamau, located in the northeast
15 of the Abitibi subprovince of Canada, help understand historic volcanic-hosted massive sulfide (VMS) deposits and
16 hydrothermal Cu-Au mineralization found there. Major faults crossed by the profiles include the Barlow fault in the north and
17 the Doda fault and the Guercheville fault in the south, all targets of this study that seeks to determine spatial relationships with
18 a known metal endowment in the area. Common-offset DMO corrections and common-offset pre-stack time migrations
19 (PSTM) were considered. Irregularities of the trace midpoint distribution resulting from the crooked geometry of both profiles
20 and their relative contribution to DMO and PSTM methods and seismic illumination were assessed in the context of the
21 complex subsurface architecture of the area. To scrutinize this contribution, seismic images were generated for offset ranges
22 of 0-9 km using increments of 3 km. Migration of out-of-plane reflections used cross-dip element analysis to accurately
23 estimate the fault dip. The seismic imaging shows the thickening of the upper crustal rocks near the fault zones along both
24 profiles. In the northern seismic reflection section, the key geological structures identified include the Barlow fault and two
25 diffraction sets imaged within the fault zone that represent potential targets for future exploration. The south seismic reflection
26 section shows rather a complicated geometry of two fault systems. The Guercheville fault observed as a subhorizontal reflector
27 connects to a steeply dipping reflector. The Doda fault dips subvertical in the shallow crust but as a steeply dipping reflection
28 set at depth. Nearby gold showings suggest that these faults may help channel and concentrate mineralizing fluids.

29 **1 Introduction**

30 Acquiring and processing a high-resolution seismic data set over Archean greenstone belts comprised of crystalline rocks
31 characterized by steeply dipping reflectors, point scatters, and multiple folded/faulted structures challenges basic assumptions
32 of the technique (Adam et al., 2000, 2003). During the past 30 years, pre-stack normal moveout (NMO) and dip moveout
33 (DMO) corrections followed by post-stack migration represented the conventional method used in most crystalline rock case
34 studies globally, with different success rates for both 2D and 3D datasets (Malehmir et al., 2012 and references therein). The
35 post-stack migration method has provided sharp images in many case studies (Juhlin 1995; Juhlin et al., 1995, 2010; Bellefleur
36 et al., 1998 and 2015; Perron and Calvert, 1998; Ahmadi et al., 2013), however, all these studies indicate low signal-to-noise
37 (S/N) ratios and scattering rather than a coherent reflection of the seismic waves. Petrophysical measurements, where available,
38 complemented with reflectivity/velocity models of the shallow crust, i.e., < 1000 m, permit a more accurate correlation of
39 reflections to geological structures (Perron et al., 1997; Malehmir and Bellefleur, 2010). The Kirchhoff pre-stack time/depth
40 migration (PSTM/PSDM) method has also been utilized in crystalline rock environments (e.g. Malehmir et al., 2011; Singh
41 et al., 2019), but computational complexity and the requirement of a detailed velocity model limited the wide application of a
42 PSTM algorithm (Fowler, 1997). In addition, strong scattering of seismic waves, low S/N ratios, and small-scale changes in
43 acoustic impedance within crystalline rock environments rendered both PSTM and PSDM algorithms less popular in a
44 crystalline rock environment (Salisbury et al., 2003; Heinonen et al., 2019; Singh et al., 2019; Braunig et al., 2020). An
45 important, somewhat neglected issue is the effect of survey geometry on processing results and if it is possible to adjust the
46 processing flow to compensate underperformance caused by the survey geometry, for example the effect of crooked survey.
47 An optimized processing flow appears essential in order to image deep mineral deposits and structures such as faults that host
48 base/precious metal deposits (Malehmir et al., 2012 and references therein).

49
50 Apart from the type of migration method (i.e., post-stack migration, PSTM or PSDM), the survey design parameters, such as
51 survey length, orientation, number of shots and receivers, shot and receiver spacing, are major factors that affect the seismic
52 illumination for both 2D and 3D surveys (Vermeer, 1998). A seismic study in Brunswick, Canada, showed that 2D seismic
53 surveys provided high-resolution seismic images of the upper crust but a 3D survey acquired over the same area failed to
54 provide more details mostly because of survey design (Cheraghi et al., 2011 and 2012). Typically, crystalline rock seismic
55 surveys in forested regions use crooked line profiling along forest tracks or logging roads for logistic and ultimately economic
56 or environmental considerations. Whereas 2D seismic processing algorithms are designed to work on straight survey lines
57 with regular offset distribution of trace midpoint (CMPs), the crooked surveys violate those assumptions and need
58 compensating strategies such as dividing the crooked survey into several straight lines, 3D swath processing, or cross-dip
59 analysis (Adam et al., 1998; Milkereit and Eaton, 1998; Adam et al., 2000; Schmelzbach et al., 2007; Kashubin and Juhlin,
60 2010). More specifically, the offset distribution affects seismic illumination during processing steps such as common-offset
61 DMO corrections or common-offset Kirchhoff PSTM algorithm (Fowler, 1997 and 1998). Proficiency of both these methods

62 demands a regular distribution of source-receiver offsets because of their sensitivity to constructive contribution of offset
63 planes (Canning and Gardner, 1998; Cheraghi et al., 2012; Bellefleur et al., 2019; Braunig et al., 2020).

64
65 This case study focuses on seismic sections along two 2D high-resolution profiles, herein named the south and north surveys
66 (Fig. 1), both acquired in 2017 in the Chibougamau area, Quebec, Canada. These profiles were acquired to aid upper crustal-
67 scale studies of metal-endowed fault structures. The Chibougamau area mostly hosts VMS (e.g., Mercier-Langevin et al.,
68 2014) and Cu-Au magmatic-hydrothermal mineralization (Pilote et al., 1997; Mathieu and Racicot, 2019). Orogenic Au
69 mineralization also documented in this area (Leclerc et al., 2017) typically relates to crustal-scale faults; hence, the importance
70 to document the geometry of major faults during exploration (Groves et al., 1998; Phillips and Powell, 2010). In order to image
71 fault systems in the Chibougamau area, we generated DMO stacked migrated sections as well as images generated with a
72 PSTM algorithm. We inclusively investigated the surveys' acquisition geometries and their effects on the DMO and PSTM to
73 optimize these processing flows according to the specific geometry. We compare the results from both methods. We show that
74 strategy and criteria used to design our processing flow favor the specific acquisition geometries of each profile in order to
75 enhance coherency of the seismic reflections in both shallow and deeper crust. To accomplish this goal, we: (1) apply pre-
76 stack DMO corrections followed by post-stack migration along both profiles; (2) analyze the application of a PSTM algorithm
77 on both surveys; (3) specifically test the CMP offset distribution and its contribution to DMO corrections and PSTM with an
78 offset range of 0-9 km; and (4) address the effect of cross-dip offsets and their relevant time shifts on the imaged reflections.
79 Our optimized application of DMO and PSTM contributes information on the geometry of the faults in the Chibougamau area,
80 which is essential to understand mineralization potential in the area and to target regions of higher prospectivity. In this study
81 we emphasize the adjustments of the processing flow that increase seismic illumination of reflectors associated with fault
82 systems. Interpretation of the fault kinematics requires inclusive field measurements and tectonic studies beyond the scope of
83 this study. Mathieu et al. (2020b) interpreted the regional seismic profile that encompasses our sections (Fig. 1) regarding the
84 geological structure and tectonic evolution down to Moho depth (~ 36 km).

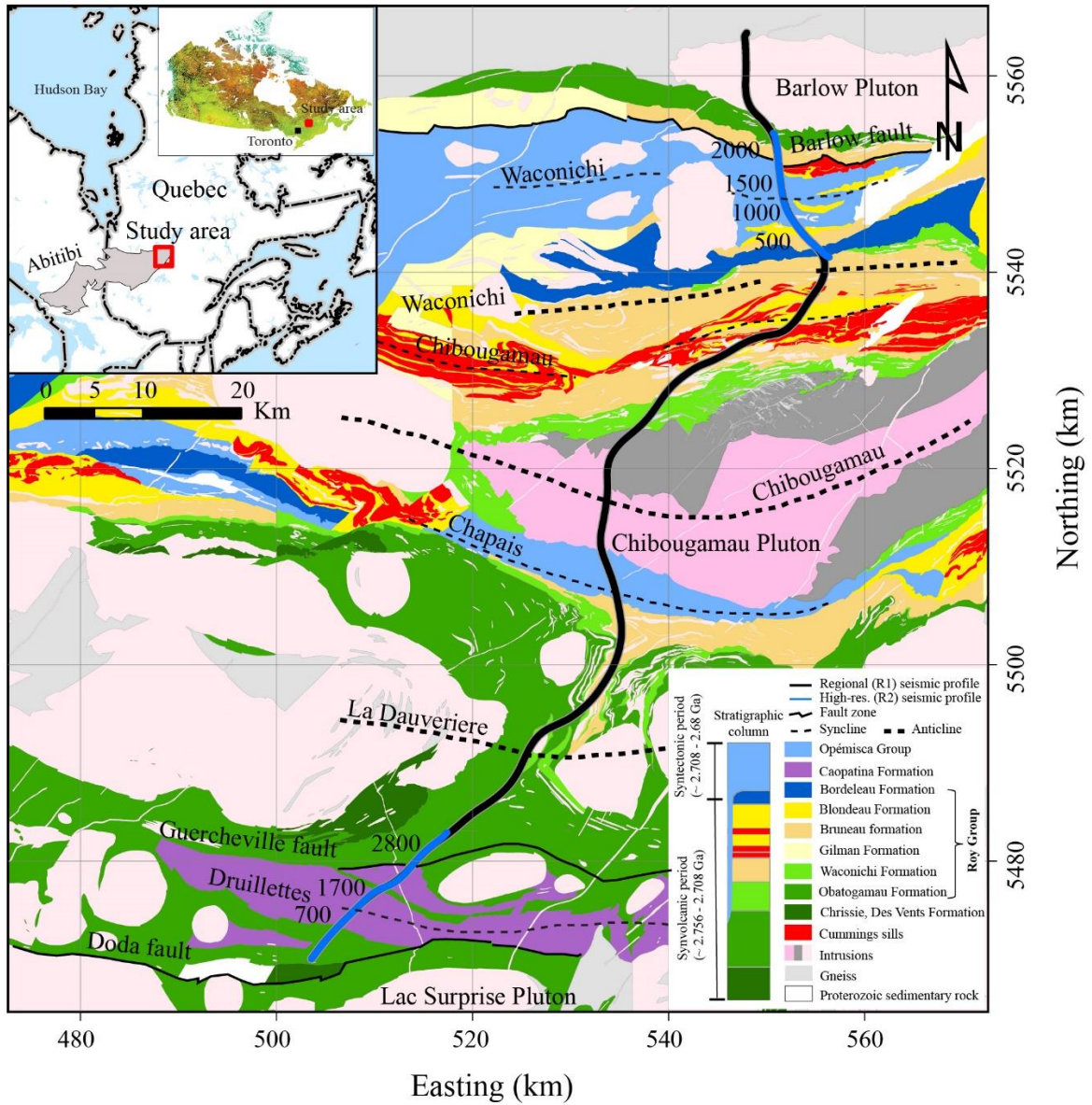
85 **2 Geological setting**

86 The Chibougamau area is located in the northeast portion of the Neoproterozoic Abitibi subprovince (Fig. 1). The oldest rocks in
87 the study area (> 2760 Ma; David et al., 2011) include mafic and felsic lava flows as well as volcanoclastic deposits of the
88 Chrissie and Des Vents formations (Fig. 1, see Leclerc et al., 2017; Mathieu et al., 2020b). These rocks are overlain by
89 sedimentary and volcanic rocks of the Roy Group, emplaced between 2730 and 2710 Ma and which constitute most of the
90 covered bedrock (Leclerc et al., 2017; Mathieu et al., 2020b). The Roy Group includes a thick (2-4 km) pile of mafic and
91 intermediate volcanic rocks topped by a thinner assemblage of lava flows, pyroclastic and sedimentary units (volcanic cycle
92 1, Leclerc et al., 2012 and 2015), as well as a pile of mafic lava flows capped by a thick (2-3 km in the north to 0.5 km in the
93 south) succession of intermediate to felsic lava flows and fragmental units interbedded with sedimentary rocks (volcanic cycle

94 2). The Roy Group is overlain by sandstone and conglomerate of the 2700-2690 Ma Opémisca Group, which accumulated in
95 two sedimentary basins (Mueller et al. 1989; Leclerc et al. 2017). The main rock exposures of the Roy Group, observed along
96 the southern profile, consist of pelitic to siliciclastic sedimentary rocks of the basin-restricted Caopatina Formation (volcanic
97 cycle 1 or Opémisca Group) and mafic to intermediate lava flows of the Obatogamau Formation (volcanic cycle 1).
98

99 The rock units around the north profile include the Bruneau Formation (mafic lava flows), the Blondeau Formation
100 (intermediate to felsic, volcanic, volcanoclastic and sedimentary deposits), and the Bordeleau Formation (volcanoclastic
101 deposits, arenite, conglomerate) of volcanic cycle 2, as well as sedimentary rocks of the Opémisca Group (Dimroth et al.,
102 1995; Leclerc et al., 2012). The major intrusions relevant in the study area are the ultramafic to mafic sills of the Cummings
103 Complex, which intrude the lower part of the Blondeau Formation (Bédard et al., 2009).
104

105 Several east-trending fault zones and synclinal/anticlinal structures are associated with Neoproterozoic deformation events in the
106 Chibougamau area (Dimroth et al., 1986; Daigneault et al., 1990; Daigneault et al., 1990; Leclerc et al., 2012 and 2017). The
107 main faults, folds and associated shistosity and metamorphism relate to a Neoproterozoic N-S shortening event (Mathieu et al.,
108 2020b and references therein). The north survey lies nearly perpendicular to the major regional structures. It crosses the west-
109 striking Barlow fault zone, a shallowly to steeply south-dipping fault zone (Sawyer and Ben, 1993; Bedeaux et al., 2020). The
110 field observations imply that the Barlow fault zone is a high-strain, back-thrust fault which separates sedimentary rocks of the
111 Opémisca Group from volcanic rocks of the Roy Group (Bedeaux et al., 2020). The north survey also crosses the Waconichi
112 syncline and the steeply dipping, east to west striking faults of the Waconichi Tectonic Zone (Fig. 1). The south survey passes
113 through the Guercheville fault zone, which intersects the Druillettes syncline (Fig. 1), and north of the east-striking Doda fault
114 zone. The Doda fault zone appears subvertical at the surface (Daigneault, 1996); the Guercheville fault dips northward at 30-
115 60 degrees but was mapped locally as a subvertical fault (Daigneault, 1996). Most of these faults form early basin-bounding
116 faults (Opémisca basins) reactivated during the main shortening event (Dimroth, 1985; Mueller et al., 1989).
117



118

119 Figure 1: The geological map of the Chibougamau study area on which major fault zones in the vicinity of the high resolution
 120 seismic profiles are marked. The regional seismic survey and the high-resolution seismic surveys in north and south of the
 121 area are located and some of the CDP locations are marked. The inset shows the location of the study area within Canada and
 122 the Abitibi subprovince.

123

124

125 3 Seismic data acquisition

126 The 2017 seismic survey in the Chibougamau area forms part of the Metal Earth exploration project in the Abitibi greenstone
127 belt (Naghizadeh et al., 2019). High-resolution seismic segments in the north and south coincide with and augment a regional
128 seismic line that crosses the main geological structures of the area (Fig. 1). Cheraghi et al. (2018) demonstrated that the
129 Chibougamau regional survey capably imaged reflections in both the upper and lower crust (down to Moho depth). Mathieu
130 et al. (2020b) interpreted the regional seismic survey to map major faults and structures in relation to geodynamic processes
131 and potential metal endowment.

132
133 The high-resolution surveys in the Chibougamau area form the focus of this study. In total, the survey acquired 2281 vibrator
134 points (VPs) along the north survey and 3126 VPs along the south survey (Fig. 1). Consistent with other high-resolution
135 surveys in the Metal Earth project (Naghizadeh et al., 2019), shot and receiver spacing were set at 6.25 m and 12.5 m,
136 respectively, with a sampling rate of 2 ms. Detailed attributes of both surveys are shown in Table 1.

137

Table 1: Data acquisition summary of the high-resolution Chibougamau north and south surveys (year 2017)

	High-resolution survey (R2)
Spread type	Split spread
Recording instrument	Geospace GSX Node
Field data format	SEGD (correlated)
Geophone type	5 Hz, single component
Source type	VIBROSEIS
No. of sources	3
Sweep length (s)	28
No. of Sweeps	1
Source starting frequency (Hz)	2
Source ending frequency (Hz)	120
Field low cut recording filter (Hz)	2
Field high cut recording filter (Hz)	207
Record length (s)	12 after cross-correlation
Sampling rate (ms)	2
Shot spacing (m)	6.25
Receiver spacing (m)	12.5
Nominal maximum offset for processing (km)	10
Number of acquired shots	2281 ^a & 3126 ^b
Survey length (km)	~15 ^a & ~19 ^b

^a North survey ^b South survey

138

139

140

141

142 3.1 Offset distribution for Kirchhoff PSTM and DMO corrections

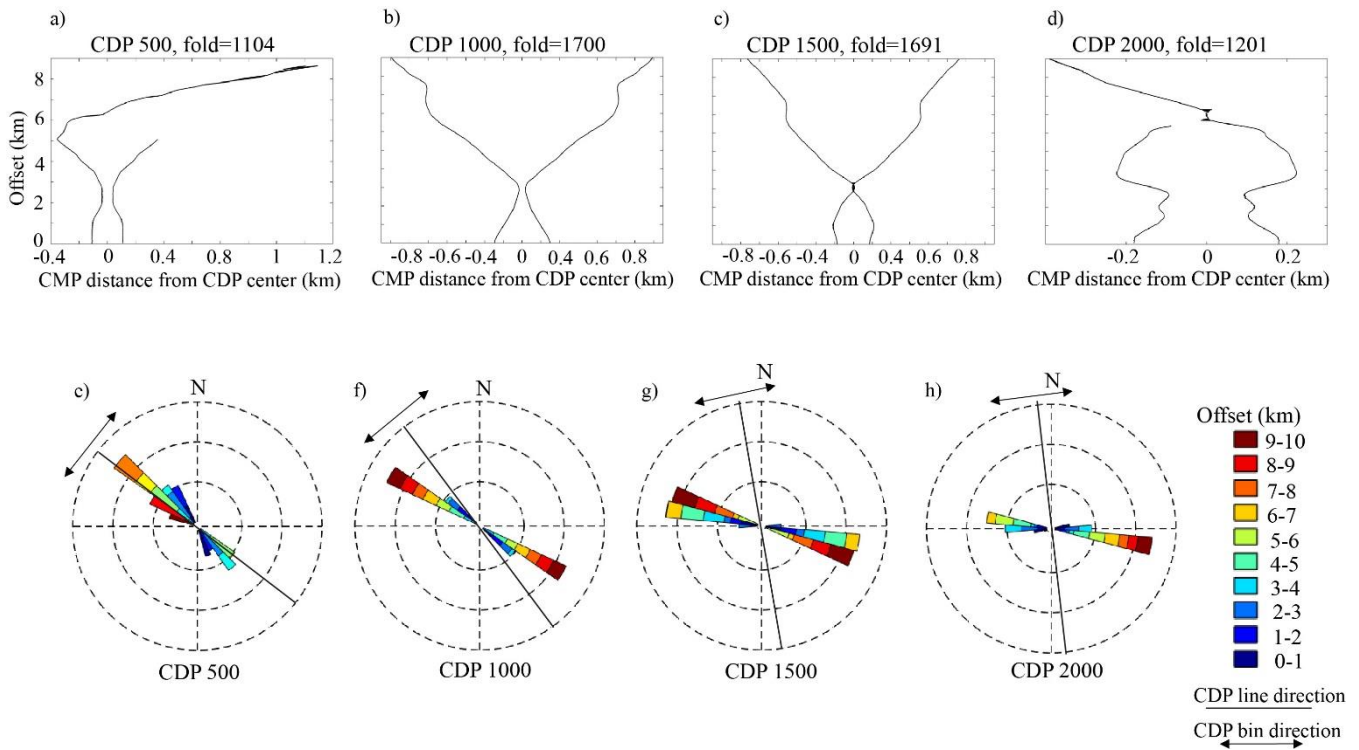
143 Based on the analysis shown in Appendix A, both profiles could record alias-free P-wave energy at velocities necessary for
144 seismic imaging in crystalline rock environments, i.e., greater than 5000 ms^{-1} . Our analysis also indicates that both profiles are
145 alias-free for shear waves and low velocity noise, e.g., ground roll. We investigated the Chibougamau profiles to evaluate
146 irregularity and optimize the application of PSTM and DMO corrections. The offset distribution forms our main criteria with
147 which to investigate the relative quality of pre- and post-stacked migrated images in the Chibougamau area based on common-
148 offset PSTM (Fowler, 1997) and common-offset DMO correction (Hale, 1991; Fowler, 1998). In Appendix A we show the
149 necessity of regular offset distribution when using common-offset DMO or PSTM (Fig. A1). Other methods of DMO or PSTM,
150 such as common-azimuth PSTM (Fowler, 1997) and common-azimuth DMO corrections should theoretically provide results
151 equal to those assuming common-offset (Fowler, 1997 and 1998). Our study did not analyze common-azimuth algorithms.
152 Besides the effect of regularity/irregularity of the survey, we also explain in Appendix A that not necessarily all CMPs
153 contribute to the DMO process (DMO illumination concept). Optimized DMO illumination can be investigated during survey
154 design by testing different subsurface models or survey geometries (Beasley, 1993). The common-offset DMO and common-
155 offset PSTM utilize similar algorithms for migration (Fowler, 1997 and 1998) and the illumination concept applies to PSTM
156 as well.

157
158 The maximum offset in these Chibougamau surveys is 10 km. We evaluated if specific offset values contribute constructively
159 or destructively in the resulting PSTM or whether they generate artifacts during the DMO corrections. We also investigated
160 PSTM and DMO corrected images at different offsets to find the offset range that optimizes subsurface illumination (Vermeer,
161 1998).

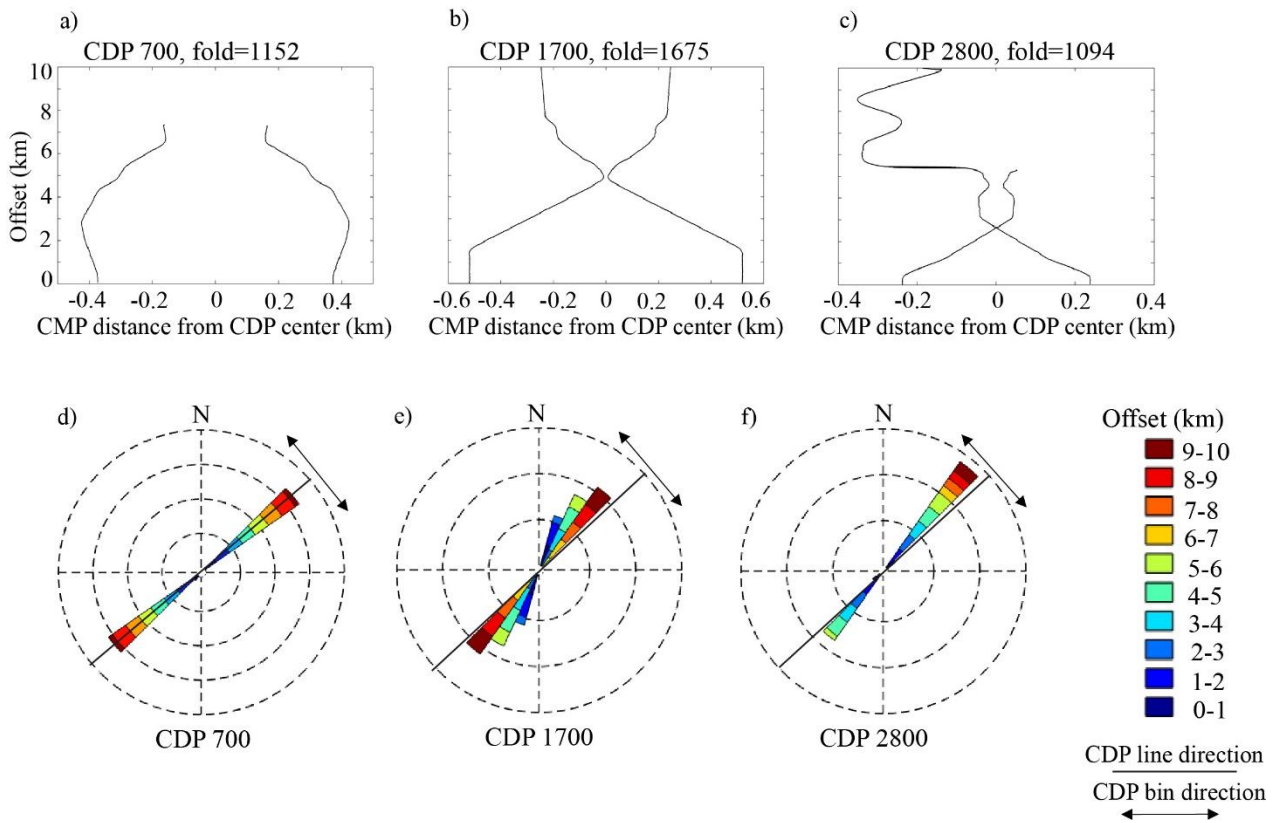
162
163 For the Chibougamau profiles, we evaluated CMP distributions within CDP bins (6.25 m, Table 2) along each survey. Figs.
164 2 and 3 present examples of CMP offset/azimuth distribution along the north and south surveys, respectively. Some of the
165 CDP bins show a regular offset distribution, for example, Fig. 2b and 2c from the north profile or Fig. 3b from the south
166 profile, respectively; note that bins located in the middle of the survey have short and long offsets equally mapped north and
167 the south of the bin center). The azimuth distribution of these CDP bins also shows a symmetric pattern relative to the CDP
168 line directions, for example, Fig. 2f and 2g from the north profile and Fig. 3e from the south profile, however, some of the
169 CDP bins however, present irregular offset and asymmetric azimuth distributions, for example, Fig. 2a, 2d, 2e, and 2h from
170 the north profile, and Fig. 3c and 3f from the south profile, respectively. These CDP bins show that longer offsets are mapped
171 unevenly in the bins resulting in an asymmetric azimuth distribution pattern. The analysis indicates that most of the irregularity
172 of offset distribution occurs due to a lack of longer offsets in those bins.

173

174 Based on the analysis shown in Figs. 2 and 3 and evaluating the distribution pattern of offset for the north and south profiles,
175 we predict an irregular distribution of CMPs would be a challenge for 2D PSTM and DMO corrections. Another challenge is
176 whether CMPs of profiles acquired in the Chibougamau area contribute constructively in DMO/PSTM towards subsurface
177 illumination considering the geometry of specific reflectors, i.e., dip and strike (more details in Appendix A). We designed
178 offset planes with offset ranges of 0-3 km, 0-6 km, and 0-9 km in order to study the survey geometry (Fig. 4). We chose these
179 offset ranges based on the analysis shown in Fig. 2 and Fig.3 and testing the effect of various offset ranges on the process of
180 post-stacked DMO and PSTM images (see Table 2 for the processing details). Offsets greater than 9 km did not increase the
181 image quality. In the north profile, CMPs with offsets ≤ 6 km cluster along the survey line (Fig. 4a and 4b), whereas many
182 CMPs with offsets greater than 6 km do not (Fig. 4c). The CMPs of the south profile lies along the survey line for all offset
183 ranges (Fig. 4d, 4e, and 4f) due to the less crooked pattern of the south profile compared to the north profile (Fig. 4).



209
 210
 211
 212 **Figure 2:** CMP offset and azimuth distribution from the north survey. The offset distribution is shown for (a) CDP 500, (b) CDP 1000, (c)
 213 CDP 1500, and (d) CDP 2000. See Figs. 1 and 4 for the location of the CDPs. The negative values for CMP distance in graphs (a)-(d) indicate
 214 CMP is located in the south of the bin center and the positive values implies that CMP is located in the north of the bin center. The azimuth
 215 distribution is shown for (e) CDP 500, (f) CDP 1000, (g) CDP 1500, and (h) CDP 2000. For each diagram shown in (e)-(h) the CDP line
 216 direction is presented. The CDP bin is perpendicular to the CDP line.



228
 229
 230
 231 **Figure 3:** CMP offset and azimuth distribution from the south survey. The offset distribution is shown for (a) CDP 700, (b) CDP 1700, and
 232 (c) CDP 2800. See Figs. 1 and 4 for the location of the CDPs. The negative values for CMP distance in graphs (a)-(c) indicate CMP is
 233 located in the south of the bin center and the positive values implies that CMP is located in the north of the bin center. The azimuth
 234 distribution is shown for (d) CDP 700, (e) CDP 1700, and (f) CDP 2800. For each diagram shown in (d)-(f) the CDP line direction is
 235 presented. The CDP bin is perpendicular to the CDP line.
 236
 237
 238
 239
 240
 241
 242
 243
 244

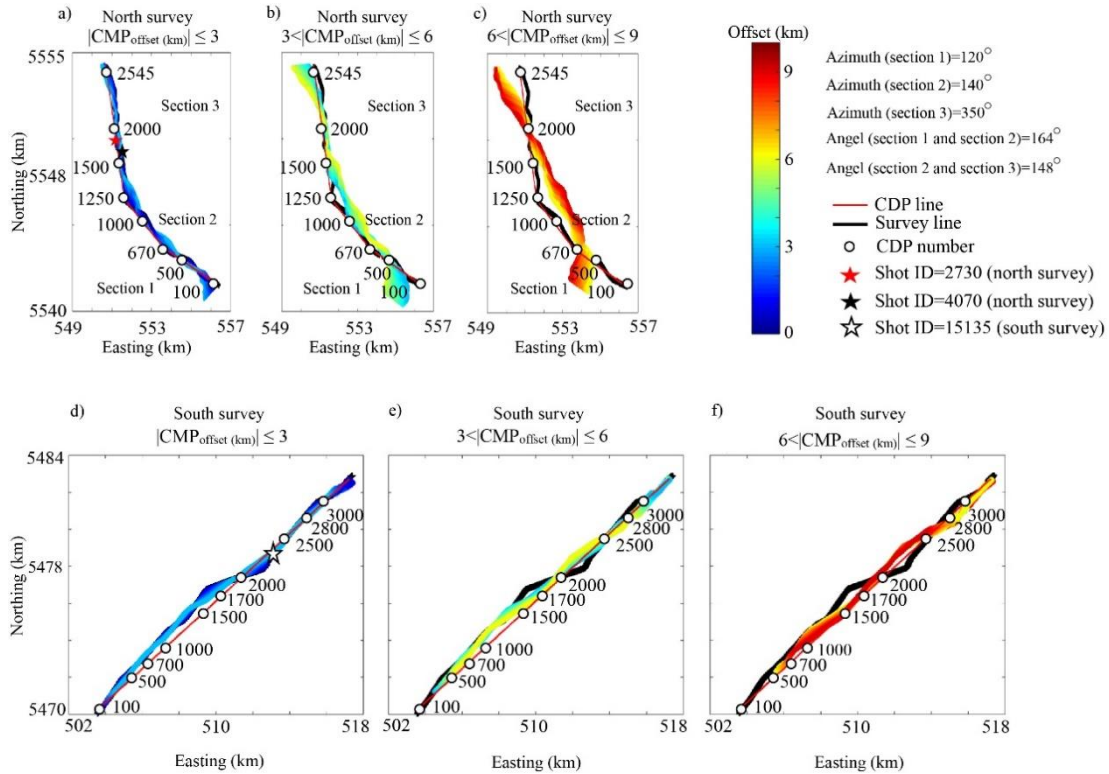


Figure 4: CMP offset distribution at range of 0-10 km for the north and the south survey in Chibougamau area. The distribution for the north survey is shown for (a) $|CMP_{offset}(km)| \leq 3$, (b) $3 < |CMP_{offset}(km)| \leq 6$, and (c) $6 < |offsetCMP_{offset}(km)| \leq 9$ and for the south survey is shown for (d) $|CMP_{offset}(km)| \leq 3$, (e) $3 < |CMP_{offset}(km)| \leq 6$, and (f) $6 < |offsetCMP_{offset}(km)| \leq 9$. The CDP line and the survey line is shown in the figure. Some shot and CDP locations are also shown. The azimuth of each section of the CDP line from the north survey and the angle between two sequential sections is presented.

Table 2: Processing parameters and attributes for the Chibougamau surveys

Chibougamau north and south surveys	
1	Read data in SEG-D format and convert to SEG-Y for processing
2	Setup geometry, CDP spacing of 6.25 m
3	Trace editing (manual)
4	First arrival picking and top muting (0-10 km offset)
5	Elevation and refraction static corrections (replacement velocity 5200 ms ⁻¹ , V ₀ 1000 ms ⁻¹)
6	Spherical divergence compensation (V^2t)
7	Median velocity filter (1400, 2500, 3000 ms ⁻¹)
8	Band-pass filter (5-20-90-110 Hz) ^{a&b}
9	Airwave filter
10	Surface-consistent deconvolution ^{c&d}
11	Trace balancing
12	AGC (window of 150 ms)
13	Velocity analysis (iterative)
14	Surface consistent residual static corrections
15	DMO corrections ^{a&b} (5500 ms ⁻¹ , offset range of 0-3 km, 0-6 km, and 0-9 km)
16	Velocity analysis (iterative at range of 5000-6500 ms ⁻¹)
17	Stacking
18	Coherency filter ^{e&f}
19	Trace balancing
20	Phase-shift time migration ^{a&b} (velocity at surface and at 4 s is 5500 m/s and 6200 m/s, respectively)
21	Kirchhoff PSTM ^{a&b} (after step 14 shown in here; offset range of 0-3 km, 0-6 km, and 0-9 km)
22	Time to depth conversion (6000 ms ⁻¹ for both north and south surveys)

^{a&b} This is applied to both north and south surveys.

^c North survey the filter length and gap is 100 ms and 16 ms, respectively

^d South survey: the filter length and gap is 100 ms and 18 ms, respectively

^e North survey: F-X deconvolution, filter length of 39 traces

^f South survey: F-X deconvolution, filter length of 19 traces

262
263
264

265 4 Data processing and results

266 We considered a pre- and post-stack processing workflow for both the north and south profiles similar to that applied by
267 Schmelzbach et al. (2007), and generated migrated DMO-corrected stacked sections, as well as Kirchhoff PSTM sections
268 (Table 2). The CMP distribution of the Chibougamau south survey lies mostly along a straight line hence a linear CDP
269 processing line was designed (Fig. 4). The CMP coverage along the north profile follows a crooked pattern hence a curved
270 CDP line that smoothly follows this geometry was used (Fig. 4). The main processing steps included attenuation of
271 coherent/random noise, refraction, and residual static corrections, sharpening the seismic data using a deconvolution filter, and
272 a top-mute to remove first arrivals.

273

274 Based on the aforementioned analysis, we considered offset ranges of 0-3 km, 0-6 km, and 0-9 km, for DMO corrections and
275 the PSTM. These steps were also deemed necessary:

- 276 • Reflection residual static corrections were applied to all shot gathers prior to the DMO corrections and PSTM
277 application (steps 1-14 in Table 2).
- 278 • Constant DMO corrections with a velocity of 5500 ms^{-1} were applied for both the north and south surveys. This
279 chosen velocity derived from several tests using various constant velocities between 5000 and 6500 ms^{-1} , with step
280 range of 100 ms^{-1} .
- 281 • After DMO corrections, velocity analysis with constant stacking velocity in the range of 5000 - 6500 ms^{-1} helped to
282 design an optimized velocity model for NMO corrections and the stacking (Table 2).
- 283 • Choosing a velocity model for PSTM was a time consuming procedure performed on the basis of trial and error. We
284 tried constant velocity models at a range of 5000 - 6500 ms^{-1} (step rate of 100 ms^{-1}) as well as the velocity model
285 applied for the DMO-NMO correction (see above). The best model adopted velocities within 90-110 % of the DMO
286 velocity model.

287
288 The DMO corrected migrated stacked sections and PSTM sections of the north and south survey appear in Figs. 5 and 6,
289 respectively. The offset range of 0-3 km reveals the most coherent reflections for both methods (Figs. 5a-b and 6a-b); the
290 velocity analysis after DMO corrections significantly improved the coherency of the reflections for the sections with an offset
291 range of 0-3 km (Figs. 5a and 6a). The migrated sections generated from offset ranges of 0-6 km and 0-9 km (Figs. 5c-f, and
292 6c-f) failed to improve the stacked sections. The stacked sections from the longer offsets (Figs. 5c, 5e, and 6c, 6e) utilized a
293 velocity model similar to the one applied to Figs. 5a and 6a for stacking after DMO correction.

294
295 The design of the north survey CDP line used three segments: CDPs 100-670 have an azimuth of 120° , CDPs 670-1250 have
296 an azimuth of 140° , CDPs 1250-2545 have an azimuth of 350° (Fig. 4). Table 3 indicates geometrical attributes of key
297 reflections imaged along the north profile. The first segment, ending at the contact between sedimentary rocks of the Bordeleau
298 Formation and mafic rocks of the Bruneau Formation, appears seismically transparent without any prominent reflections (Fig.
299 5a and 5b). Labeled in Fig. 5, chn1, chn2, and chn3 mark the major reflections imaged in the upper crust. The most prominent
300 reflection package of the north survey is chn3, with an apparent width of approximately 3 km on the surface and an apparent
301 thickness of approximately 2 km (see Table 3 for detailed attributes). Reflections chn4, chn5, and chn6 image at depths greater
302 than 2 km could be related to structure at the southern boundary of the Barlow pluton (Fig. 1). The horizontal reflection
303 chn_diff, with a horizontal length of approximately 1 km, appears in the DMO staked migrated section (Fig. 5a) and also
304 weakly in the PSTM section (Fig. 5b). Reflection chn_diff intersects the chn4 reflections. The apparent geometry of the
305 chn_diff reflection in the migrated sections would suggest a curved feature or else a diffracted wave that collapsed to a
306 horizontal reflection after the migration.

307

308 The Chibougamau south survey mostly traverses mafic to intermediate lava flows of the Obatogamau Formation and
309 sedimentary rocks of the Caopatina Formation (Fig. 6). The DMO stacked migrated (Fig. 6a) and PSTM sections (Fig. 6b)
310 both show steeply dipping and subhorizontal reflections in the upper crust, but upper crustal reflections in the DMO stack
311 section (Fig. 6a) show more coherency than those of the PSTM (Fig. 6b). Therefore, the DMO stack facilitates correlation
312 with the surface geology. Reflection packages chs1, chs2, and chs3 mark the most prominent features in the upper crust imaged
313 along the south survey. The deeper reflections include reflection chs4 at depths greater than 2 km and two packages of steeply
314 dipping reflections chs5 and chs6 at depths greater than 6 km, together extended along 18 km length of the survey. Table 3
315 summarizes the geometrical attributes of these reflections.

316 **5 Cross-dip analysis**

317 The analysis performed on offset distribution indicated that selecting a proper offset range, here 0-3 km, was crucial for both
318 DMO corrections and PSTM. Another factor that could affect the imaging involves CMP locations relative to CDP bin centers.
319 For the Chibougamau surveys, the maximum CMP offset perpendicular to the CDP line was about ± 0.4 km when an offset
320 range of 0-3 km is considered for processing (Fig. 4a and 4d). The 3D nature of subsurface geology around a crooked-line
321 survey requires that out-of-plane features be evaluated, accounting for the time shifts from these features. When out-of-plane
322 CMPs scatter/reflect seismic waves from steep structures off the CDP line (cross-dip direction) exist, cross-dip analysis
323 addresses time shifts of those structures and adjusts accordingly (for example, Larner et al., 1979; Bellefleur et al., 1995;
324 Nedimovic and West, 2003; Rodriguea-Tablante et al., 2007; Lundberg and Juhlin, 2011; Malehmir et al., 2011). Calculated
325 time delays, called cross-dip move out (CDMO) and treated as static shifts can be applied to both NMO or DMO corrected
326 sections (Malehmir et al., 2011; Ahmadi et al., 2013). CDMO is sensitive to both velocity and the cross-dip angle applied,
327 however, the variation of the angle appears more crucial for hard rock data (Nedimovic and West, 2003).

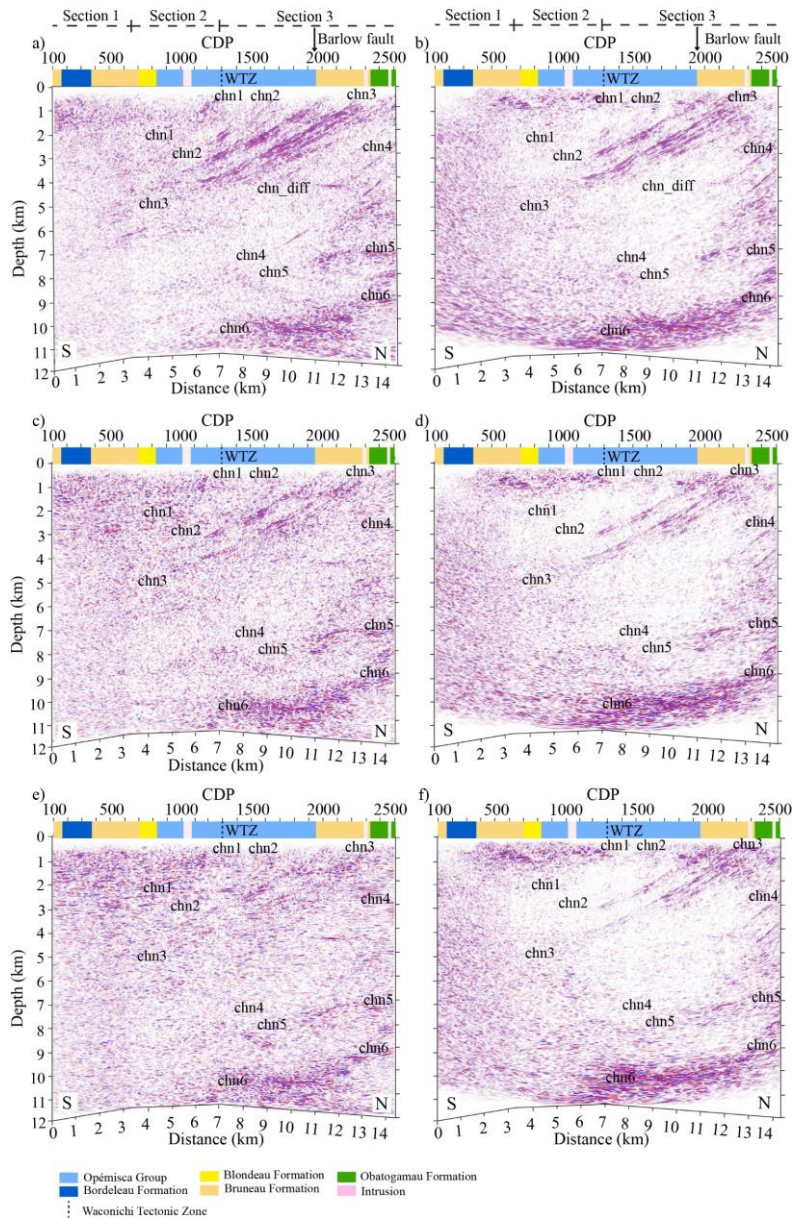
328
329 In this Chibougamau case study, we used DMO corrected sections (constant velocity of 5500 ms^{-1} , Table 2) for CDMO
330 analysis, similar to a study by Malehmir et al. (2011). First, the CMP offset relevant to a bin center and perpendicular to the
331 CDP line was calculated (Fig. 4). CDMO calculated for dip angles varying from 40° to the west to 40° to the east with a step
332 rate of 2° was then applied to DMO corrected CMPs. Finally, we stacked DMO-CDMO corrected traces using a velocity model
333 designed from the one applied after DMO corrections during standard processing (Table 2). Further velocity analysis checked
334 if the coherency of the reflections could be improved, but the new velocity model, where different, showed less than ± 5 %
335 changes from the input model. Some example of the CDMO analysis applied to the Chibougamau surveys appears in Figs. 7-
336 9. Table 3 summarizes which CDMO elements (i.e., toward east or west or no cross-dip) increase the coherency of the
337 reflections when considering time delays associated with out-of-plane reflections.

338

339 In the Chibougamau north survey, most of the seismic reflectivity is observed at CDPs 700-2500 (Figs. 4 and 5), which include
340 segments 2 and 3 of the processing line; as such, we have performed the CDMO analysis for those two sections, separately. In
341 segment 2 (CDPs 670-1250, Fig. 4), reflections chn1, chn2, and chn3 appear with no cross-dip element applied (Fig. 7c). The
342 CDMO analysis of segment 2 (Fig. 7) did not reveal any significant reflectivity in the deeper part of the section, i.e., 2-4 s (~
343 6-12 km, mid-crust). The CDMO analysis along segment 3 is shown as Fig. 8. Applying the westward CDMO increased the
344 coherency of diffraction chn_diff. A diffraction package imaged at depths lesser than 1 s (dashed area in Fig. 8c) is not imaged
345 in the migrated sections (Fig. 5). One horizontal reflection at a depth of approximately 11 km (~ 3.5 s) between CDPs 1600-
346 2000 located within reflection package chn6 shows almost equal coherency independent of the applied cross-dip to east or
347 west (Fig. 8).

348
349 The CDMO analysis in the south profile was more challenging because of interfering reflections that dip steeply to the north
350 and to the south (Fig. 6). The CDMO analysis results for the south survey appear in Fig. 9 and Table 3. The reflection chs2
351 displays a complicated CDMO analysis (Fig. 9). With cross-dip towards the west assumed, reflection chs2 becomes less steep
352 (Fig. 9). Assuming a cross-dip of 30° to the west, chs2 dips 20° to the south (Fig. 9a) whereas with no CDMO correction it
353 dips 40° to south and features less continuity (Fig. 9c). With any cross-dip element towards the east applied, chs2 dips more
354 steeply. Reflection chs2 dips 50° to the south with a cross-dip element of 40° to the east applied (Fig. 9f). CDMO analysis for
355 reflection chs3, presents another complicated scenario. This reflection shows the same dip (40°) and its coherency improves
356 with increasing west cross-dip element (Fig. 9a-c). On the other hand, with an east cross-dip element applied, reflection chs3
357 becomes less steep (for example 20° in Fig. 9e versus 40° in Fig. 9c), and its coherency decreases (Fig. 9c-f).

358
359
360
361
362
363
364
365
366
367
368
369
370
371



372
 373
 374
 375
 376
 377
 378
 379
 380

Figure 5: Migrated sections from the north survey with considering offset plane at range of 0-9 km. DMO corrected migrated section and PSTM section shown in (a) and (b) for offset plane of 0-3 km, respectively; and shown in (c) and (d) for offset plane of 0-6 km, respectively; and shown in (e) and (f) for offset plane of 0-9 km, respectively. Prominent reflections are imaged in shallow and deep zone of the sections. For interpretation of chn1, chn2, chn3, chn4, chn5, chn6, and chn_diff see text. The survey includes 3 sections which are projected on top of the image. The rock units along the survey path are projected on top of each section with no dip in the contacts implied. The surface location of the Barlow fault is marked on top of the section.

Table 3: Geometrical attributes of reflections imaged in Chibougamau area

Reflection name	CDP location	Dip (°)	Dip direction	Subsurface extension	CDMO	
					Segment 2	Segment 3
North profile						
chn1 ^{PF}	800-1300	40	South	Near surface down to ~ 2 km	No cross-dip	-
chn2 ^{PF}	900-1700	40	South	Near surface down to ~ 3 km	10° to east	10° to east
chn3 ^{GC,BF}	1000-2500	30	South	Near surface down to ~ 5 km	10° to east	10° to east
chn4 ^{PF}	1500-2600	40	South	2-7 km	-	No cross-dip
chn5 ^{GC}	1800-2600	Subhorizontal	South	7-12 km	-	12° to west
chn6 ^{GC}	1400-2600	Subhorizontal	South	7-12 km	-	30° to west
chn_diff	1900-2000	Horizontal	-	At depth of ~ 4 km	-	12° to west
South profile						
chs1 ^{GC}	1600-1700	40	South	Near surface down to ~ 3 km	No cross-dip	
chs2 ^{GC,PF,GV}	1700-2800	40	South	1-5 km	Complicated structure for CDMO analysis*	
chs3 ^{GC}	600-1800	40	North	Near surface down to ~ 7 km	Complicated structure for CDMO analysis*	
chs4 ^{GC,PF,DF}	100-800	30	North	2-5 km	30° to west	
chs5 ^{GC}	100-1700	Steeply dipping	North	6-9 km	30° to west	
chs6 ^{GC}	1700-2700	Steeply dipping	South	6-9 km	10° to east	

*The reflection package shows varying dip with cross-dip to east or west applied. See text for more details.

^{GC} The geological contact ^{PF} The possible fault ^{BF} The Barlow fault ^{GV} The Guercheville fault ^{DF} The Doda fault

382

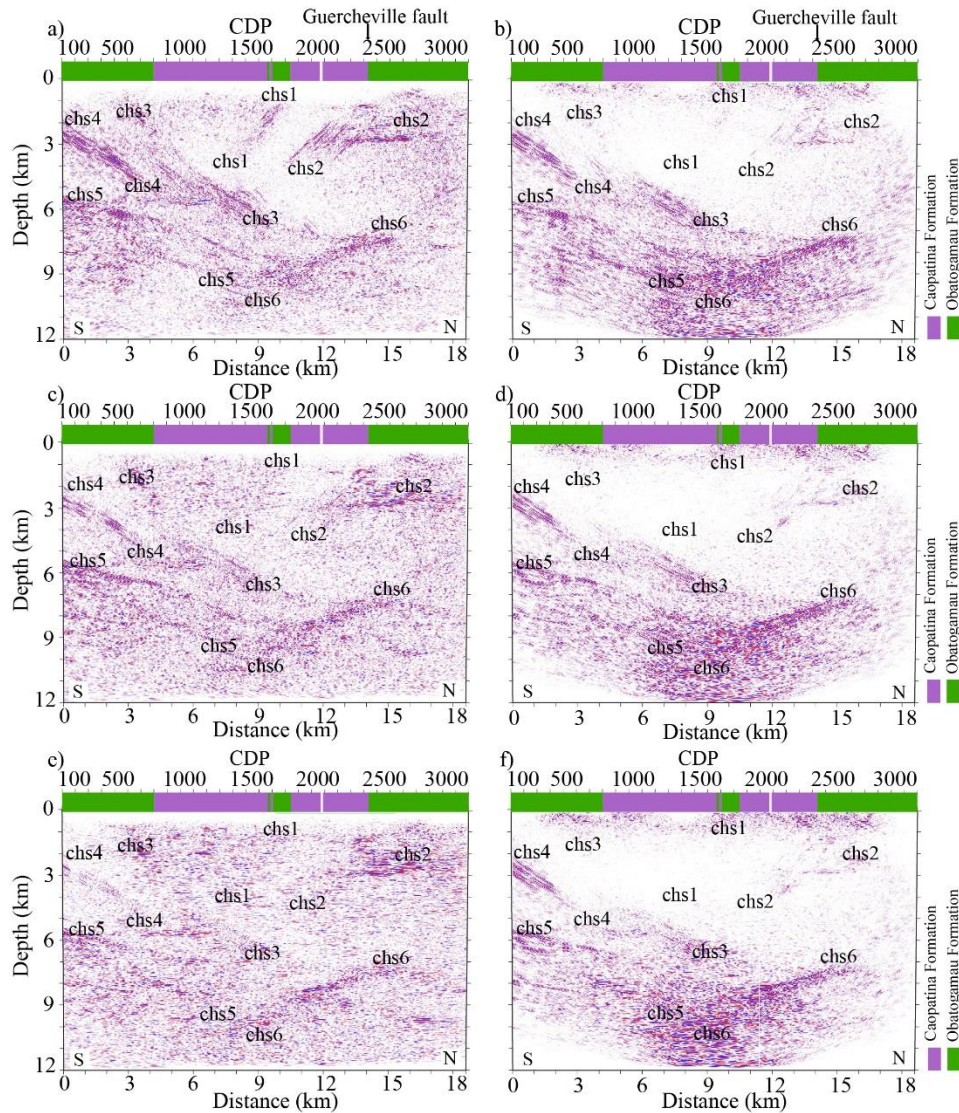
383 6 Discussion

384 The high resolution seismic profiles acquired in the Chibougamau area present an essential case study to address the challenges
385 of the application of the method in a crystalline rock environment. One goal of our research was to adjust the processing flow
386 to improve subsurface illumination. To achieve this, we analyzed the performance of common-offset DMO and PSTM.
387 Another aspect of our research involved geologic interpretation of the seismic sections, especially around the fault zones, that
388 could unravel potential zones for detailed mineral exploration. Detailed study of fault zones including age, kinematic, and
389 alteration could provide more insight about mineral exploration, but requires inclusive field investigation and petrography
390 beyond the scope of our present study.

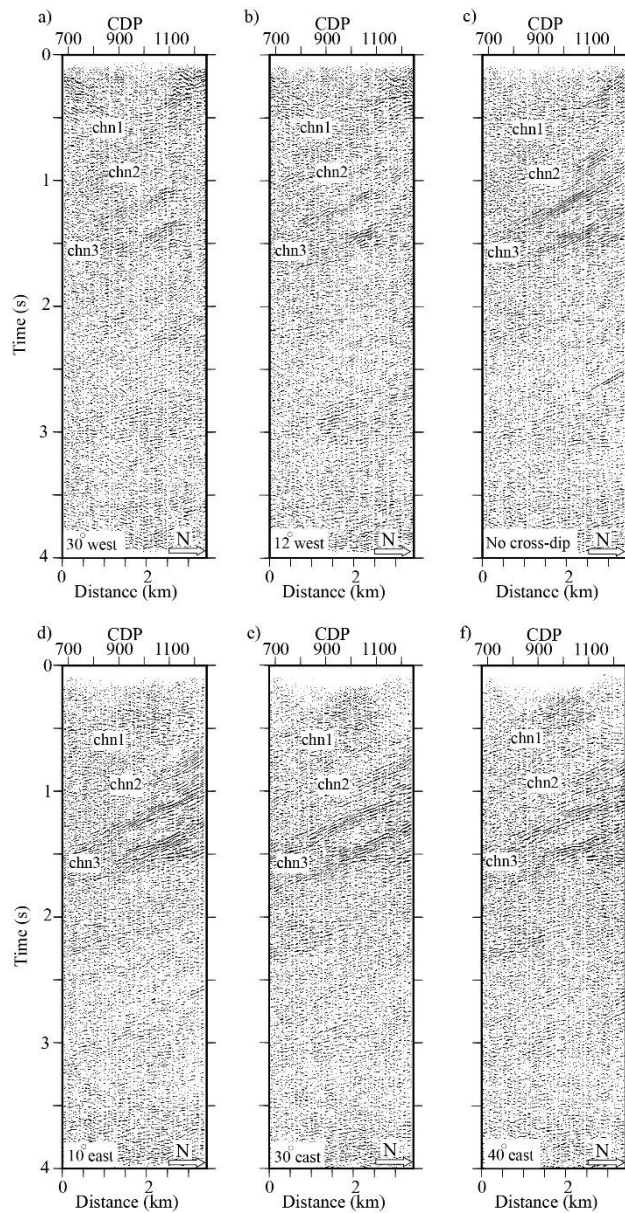
391 6.1 The effect of survey geometry on seismic imaging

392 The analysis performed on common-offset DMO and PSTM sections showed the importance of offset range and CMP
393 distribution on CDP bins and whether CMPs offsets at ranges of 0-10 km could all contribute constructively in the resulting
394 images (Figs. 5 and 6). The analysis summarized in Figs. 2 and 3 indicates that the survey geometry resulted in irregular offset
395 distribution in CDP bins, especially for longer offsets. The immediate effect of this irregularity was under-performance of
396 DMO and PSTM for the longer offsets (Figs. 5 and 6). We explain in Appendix A that several factors including spatial
397 attributes of the reflectors (i.e., dip and strike) and survey geometry (i.e., shot and receiver location) define the DMO
398 illumination. Ideally, the impact of known subsurface architecture on DMO illumination should be analyzed before data
399 acquisition at the survey design stage (Beasley, 1993; Ferber, 1997). In our study, the DMO illumination criteria can be

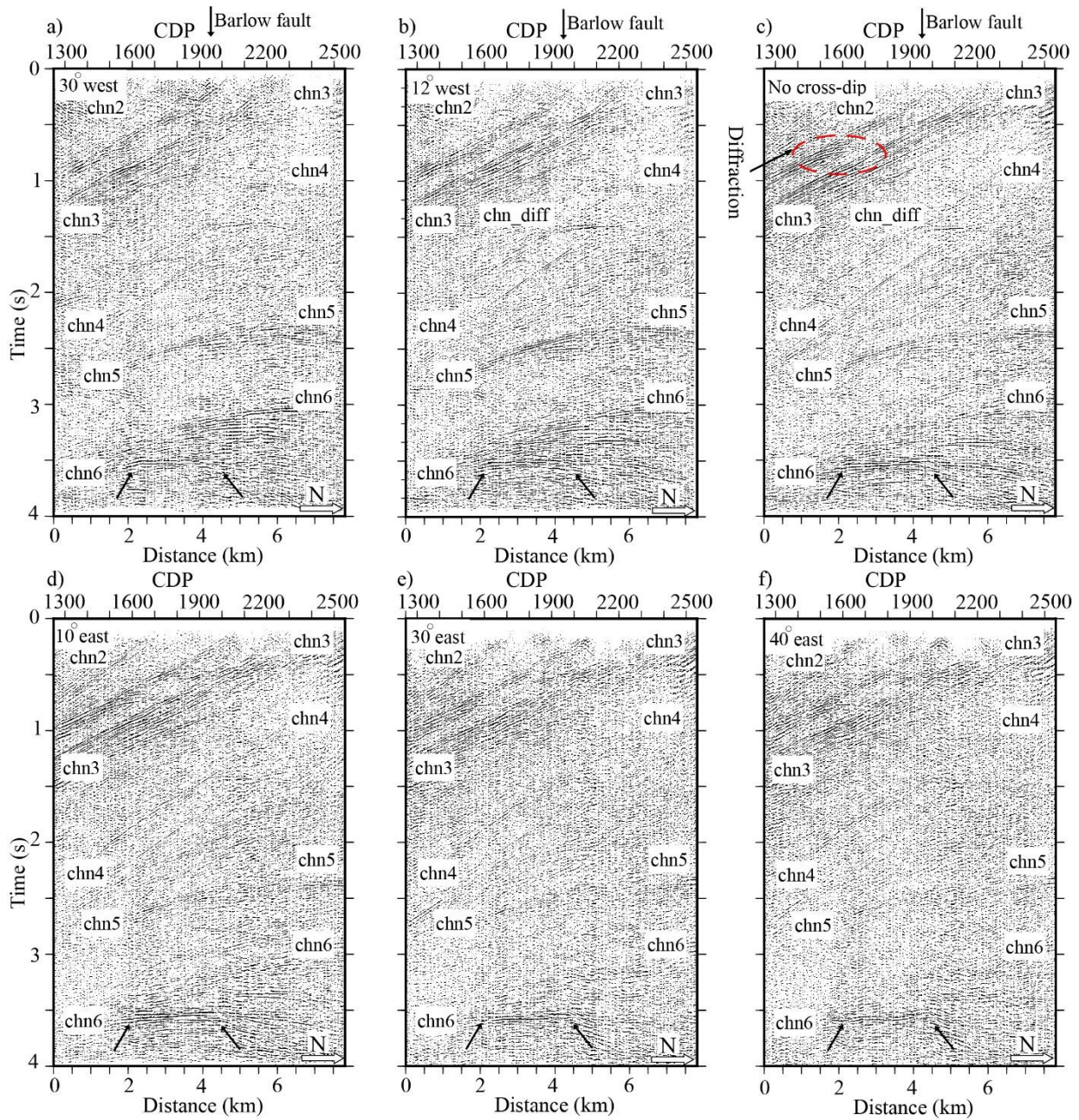
400 extended to the PSTM process because common-offset DMO correction and common-offset PSTM utilize similar algorithms
 401 for migration (Fowler, 1997 and 1998).
 402



403
 404
 405 **Figure 6:** Migrated sections from the south survey with considering offset plane at range of 0-9 km. DMO corrected migrated section and
 406 PSTM section shown in (a) and (b) for offset plane of 0-3 km, respectively; and shown in (c) and (d) for offset plane of 0-6 km, respectively;
 407 and shown in (e) and (f) for offset plane of 0-9 km, respectively. Prominent reflections are imaged in shallow and deep zone of the sections.
 408 For interpretation of chs1, chs2, chs3, chs4, chs5, and chs6 see text. The rock units along the survey path are projected on top of each section
 409 with no dip in the contacts implied. The surface location of the Guercheville fault is marked on top of the section.

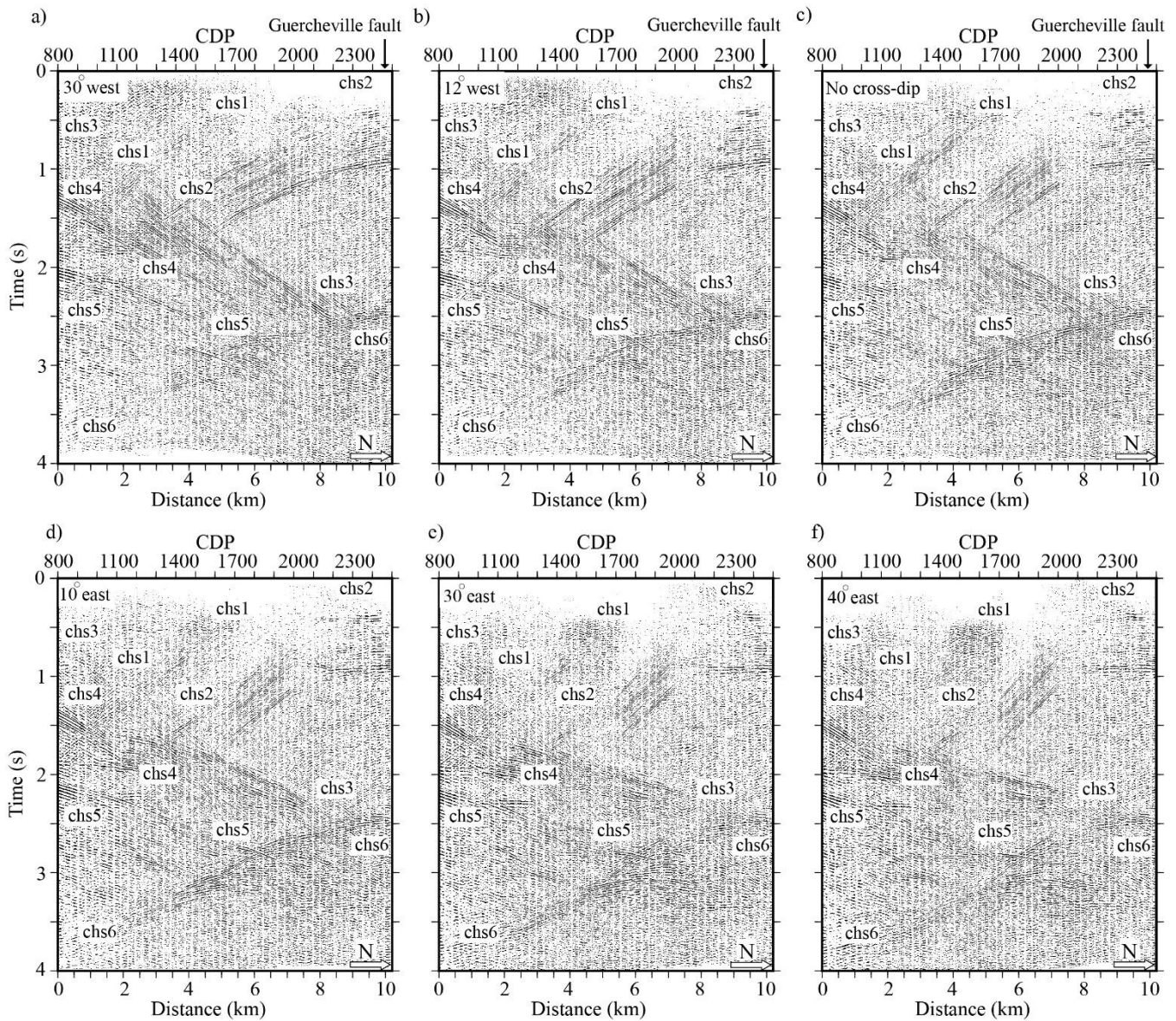


410
 411 **Figure 7:** CDMO analysis for the north survey along section 2 (see Fig. 4 for the location of the section). (a) DMO corrected stacked section
 412 with cross-dip element of 30° to west applied. (b) DMO corrected stacked section with cross-dip element of 12° to west applied. (c) DMO
 413 corrected stacked section with no cross-dip element applied. (d) DMO corrected stacked section with cross-dip element of 10° to east applied.
 414 (e) DMO corrected stacked section with cross-dip element of 30° to east applied. (f) DMO corrected stacked section with cross-dip element
 415 of 40° to east applied. See text for interpretation of marked reflections.



419
 420
 421
 422
 423
 424
 425

Figure 8: CDMO analysis for the north survey along section 3 (see Fig. 4 for the location of the section). (a) DMO corrected stacked section with cross-dip element of 30° to west applied. (b) DMO corrected stacked section with cross-dip element of 12° to west applied. (c) DMO corrected stacked section with no cross-dip element applied. (d) DMO corrected stacked section with cross-dip element of 10° to east applied. (e) DMO corrected stacked section with cross-dip element of 30° to east applied. (f) DMO corrected stacked section with cross-dip element of 40° to east applied. See text for interpretation of marked reflections and diffractions. The surface location of the Barlow fault is presented on top of the section.



426
427
428
429
430
431
432
433
434

Figure 9: CDMO analysis for a part of the south survey around the Guercheville fault. (see Fig. 4 for the location). (a) DMO corrected stacked section with cross-dip element of 30° to west applied. (b) DMO corrected stacked section with cross-dip element of 12° to west applied. (c) DMO corrected stacked section with no cross-dip element applied. (d) DMO corrected stacked section with cross-dip element of 10° to east applied. (e) DMO corrected stacked section with cross-dip element of 30° to east applied. (f) DMO corrected stacked section with cross-dip element of 40° to east applied. The surface location of the Guercheville fault is shown on top of the section. See text for interpretation of marked reflections.

435

436

437 In the Chibougamau area, our strategy adjusted DMO and PSTM to find an offset range that better serves the concept of
438 regularity. We performed detailed velocity analysis to design a velocity model producing the highest illumination. The DMO
439 and PSTM images with an offset range of 0-3 km provided the most convincing images for both profiles when considering
440 only reflection coherency (Figs. 5a-b and 6a-b). Artifacts in the form of subhorizontal features appear in DMO sections where
441 the longer offsets (0-6 km, and 0-9 km) are used to create the images (Figs. 5c, 5e, 6c, and 6e). Such artifacts disguise the
442 DMO images of the surveys, especially in the upper crust in depths less than 6 km, and indicate a destructive contribution of
443 CMPs in the DMO process as previously recognized in other surveys acquired in crystalline rock environments (Cheraghi et
444 al., 2012). PSTM images of the both profiles (Figs. 5b, 5d, and 5f and 6b, 6d, and 6f) had less capability to image steeply-
445 dipping reflection at depths less than 6 km. This could relate to either a lack of a detailed velocity model or an inadequate
446 contribution of CMPs, especially for longer offsets. PSTM images of longer offsets do show an adequate capability of
447 preserving deeper reflections, for example, reflection chn6 in Fig. 5d and 5f (c.f., Fig. 5c and 5e, respectively) and reflections
448 chs5 and chs6 in Fig. 6d and 6f (c.f., Fig. 6c and 6e, respectively).

449 **6.2 Seismic interpretation in Chibougamau area**

450 Both surveys imaged several packages of reflections from the near-surface down to 12 km (upper crust, Figs. 5 and 6). As
451 noted before, DMO stacked migrated sections and PSTM images with an offset range of 0-3 km presented more coherent
452 reflections, thus our interpretation used the images shown in Figs. 5a-b and 6a-b, respectively. The geometrical attributes of
453 the reflections are shown in Table 3. The geological map (Fig. 1) shows several fault zones in the Chibougamau area intersected
454 by each profile. Both profiles show reasonable correlations of seismic reflections to the surface geology at depths less than 6
455 km. Some imaged reflectors may match known faults. Here, the aim is to get geometrical attributes on the planar structures
456 being imaged and to discuss possible relationships to mapped faults (Fig. 1) without further investigation of the kinematic,
457 alteration, age and mineralogy which are not within the scope of this study. This helped us to map the major fault zones and
458 interpret the seismic sections. The CDMO analysis also served as a tool to investigate out-of-plane apparent dip of the reflection
459 packages. The interpretation of each seismic profile follows.

460 **6.2.1 Seismic interpretation along the north profile**

461 Migrated sections of the north profile (Fig. 5) show a general trend of south-dipping reflectors without any conflicting dips in
462 the upper crust (depths less than 6 km). The contact of the Bruneau Formation (mafic volcanic rocks) with Opémisca Group
463 (sedimentary rocks) and Obatogamau Formation (mafic to intermediate volcanic rocks) is likely the major cause of the
464 reflectivity in the upper crust (chn1, chn2, chn3, and probably chn4 in Fig. 5). The reflection chn4 lies within a seismically
465 transparent zone and also separates the deeper subhorizontal reflections sets (chn5 and chn6, Fig. 5) from the upper crust

466 steeply dipping reflections. The thickening of the upper crust rocks around the reflection set chn3 correlates the Barlow fault
467 and the regional Waconichi syncline cored by a successor (Opémisca) basin (Fig. 5) (Mathieu et al., 2020b).
468

469 Reflection chn1 (Fig. 5, Table 3) at CDP 1300 projects to the surface within the sandstones and conglomerates of the Opémisca
470 Group and may correspond to internal structure such as an unconformity or small fault that is part of the Waconichi Tectonic
471 Zone or lithological variations inside the Opémisca Group. Similar to reflection chn1, Reflection chn2 (Fig. 5, Table 3)
472 correlates with local structure, i.e., small fault or mafic/ultramafic lithology in outcrops of Opémisca Group rocks.
473

474 Reflection package chn3 occupies 3 km of the seismic section (Fig. 5 and Table 3) and helps to interpret both the Barlow fault
475 and geological contacts in north of the Chibougamau area (Fig. 1 and Fig. 5). At CDP 1950 reflections within chn3 (see Table
476 3 for geometric attributes) correlate to the contact between sedimentary rocks of Opémisca Group and mafic lava flows of the
477 Bruneau Formation. This contact is overprinted by the Barlow fault at the surface (Sawyer and Ben, 1993) and the migrated
478 images (Fig. 5a-b) suggest that the fault dips at 30° to the south (Table 3; see also Bedeaux et al., 2020). The Barlow fault
479 zone strikes east-west and the northern seismic profile makes an angle of $\sim 130^\circ$ where it crosses the fault zone (Fig. 1). This
480 would suggest that the true dip of the fault zone is steeper than the apparent dip imaged in the migrated section (i.e., greater
481 than 30° ; Fig. 5a-b). Reflections within chn3 also correlate with the contact of the Bruneau Formation (mafic rocks) and
482 Obatogamau Formation (mafic to intermediate lava flows) at CDP 2400. We previously noted that the reflection package chn3
483 forms the most coherent package along the north survey in the upper crust. The CDMO analysis around reflections chn3 (Fig.
484 8) would suggest a 0° - 10° strike towards the east (Fig. 8c and 8d, Table 3). Furthermore, these reflections became weakly
485 imaged assuming a CDMO towards the west (Fig. 8a and 8b) or toward the east at dips greater than 10° (Fig. 8e and 8f). Thus
486 reflection set chn3 most likely originates within a complex structure, off the plane of the north profile. It is possible that the
487 Cumming sills located east of the northern profile and near the Barlow fault contribute to the structures imaged as reflection
488 package chn3. Finally, the CDMO analysis also indicates an eastward apparent dip for other upper crustal reflection packages
489 of the north profile (chn1 and chn2, Table 3). The seismic images shown in Fig. 5 and Fig. 8 suggest that the Barlow fault
490 forms part of a steeply dipping structure (dip $> 30^\circ$) that dips slightly towards the east.
491

492 Unless the north profile was extended beyond the CDP 2600 (Figs. 1 and 5) we cannot be sure that the reflection set chn4
493 correlates to surface geology. The regional survey in the Chibougamau area (Mathieu et al., 2020b) does not show any surface
494 correlation to these reflections at depth. The CDMO analysis did not show any prominent cross-dip elements for this reflection
495 (Table 3). We noted that reflection chn4 could be associated with the southern structure of the Barlow pluton. Deeper reflection
496 packages (greater than 6 km) do not correlate to surface geology; subhorizontal reflections chn5 and chn6, at depths of 7-12
497 km, have no clear geological interpretation. These reflections show westward cross-dip elements (Table 3). Mathieu et al.
498 (2020b) suggested that reflectors at those depths in northern Chibougamau represent imbrication between the Opatica plutonic
499 belt and the Abitibi greenstone belt.

500

501 The DMO stacked section of the north survey and CDMO analysis also provided insights into the diffractions within the upper
502 crust. Diffractions could be generated from spherical/elliptical (ore) bodies within fault zone structures and they are potentially
503 relevant to mineral exploration (Malehmir et al., 2010; Cheraghi et al., 2013; Bellefleur et al., 2019). Our analysis suggests
504 the utility of considering DMO stacked sections with cross-dips to image diffractions better. The imaged diffraction enhances
505 understanding of chn3 and its interest to exploring for massive sulphide deposits.

506

507 CDMO analysis revealed a more coherent image of the diffraction chn_diff assuming a cross-dip of 12° to west (Fig. 8b and
508 Table 3). The diffraction chn_diff shows a larger width (~ 2 km in the plane of the DMO stacked section) compared to the
509 diffraction within reflection package of chn3 (Fig. 8c). The shallower diffraction appears clearer with no cross-dip element
510 (dashed area in Fig. 8c) and thus seems to be located in the plane of the seismic profile with no lateral dip. It is not imaged in
511 the migrated section (Fig. 5a) mainly because its low amplitude did not survive a migration that collapsed diffraction energy.

512

513 In order to scrutinize the diffraction imaging capability, we compare an enlarged section of the upper crust of the Chibougamau
514 north survey (shallower than 1.5 s) with no cross-dip applied (Fig. 8c) with a section with cross-dip 12° to the west applied
515 (Fig. 8b) in Figs. 10 and 11, respectively. Figure 10a clearly shows the diffraction tail imaged within reflection package chn3
516 at CDP 1600 (marked with red dashed ellipse).

517

518 A zoomed view of the diffraction chn_diff in a section with a cross-dip element of 12° to west is shown in Fig. 11. Similar to
519 the analysis shown in Fig. 10, we visually checked the shot gathers around CDP locations where chn_diff was imaged (CDPs
520 1900-2200). Shot gather 2730 (Fig. 4a for location) is shown as an example. This shot gather imaged a package of reflections
521 interpreted as chn3 and also diffracted events at approximately 1.5 s in CDP locations where chn_diff was expected to be
522 imaged (see CDP 2088 marked as the apex of the diffraction in Fig. 11b).

523

524 Diffractions are easy to miss and require a focused visual inspection of DMO stacked sections and shot gathers (Malehmir et
525 al., 2010; Cheraghi et al., 2013). The analysis of DMO/CDMO stacked images shown in Figs. 5 and 8 helped to image both
526 out of plane and planar diffractions (Fig. 8b and 8c, respectively) near the Barlow fault. In particular, the CDMO stack image
527 enhanced the illumination of diffraction chn_diff (Fig. 8b). These diffractions can be considered a target of more detailed
528 exploration.

529 **6.2.2 Seismic interpretation along the south profile**

530 The south profile shows more complexity in the upper crust where both north and south dipping reflections are imaged (Fig.
531 6). It seems that the lithological contact of the Obatogamau Formation (intermediate to mafic rocks) and the Caopatina
532 Formation (sedimentary rocks) is the main cause of the reflectivity along the south profile in the upper crust (Fig. 6). The

533 volcanic-sedimentary reflection packages in the upper crust (chs1, chs2, and chs3) and deeper reflection packages (chs4, chs5,
534 chs6) depict a synform structure along the south profile. The geometry of this structure includes the south dipping reflection
535 in the north of the profile and north dipping reflection in the south (Fig. 6). Similar to the north profile (Fig. 5), the upper
536 crustal rocks around the reflection sets chs1, chs2, chs3, and chs4 (Fig. 6) are approximately 6 km thick.

537

538 Reflection chs1 (Fig. 6, Table 3) at CDP 1700 likely correlates with the contact between pelitic to siliciclastic sedimentary
539 rocks of the basin-restricted Caopatina Formation and mafic to intermediate lava flows of the Obatogamau Formation.

540

541

542

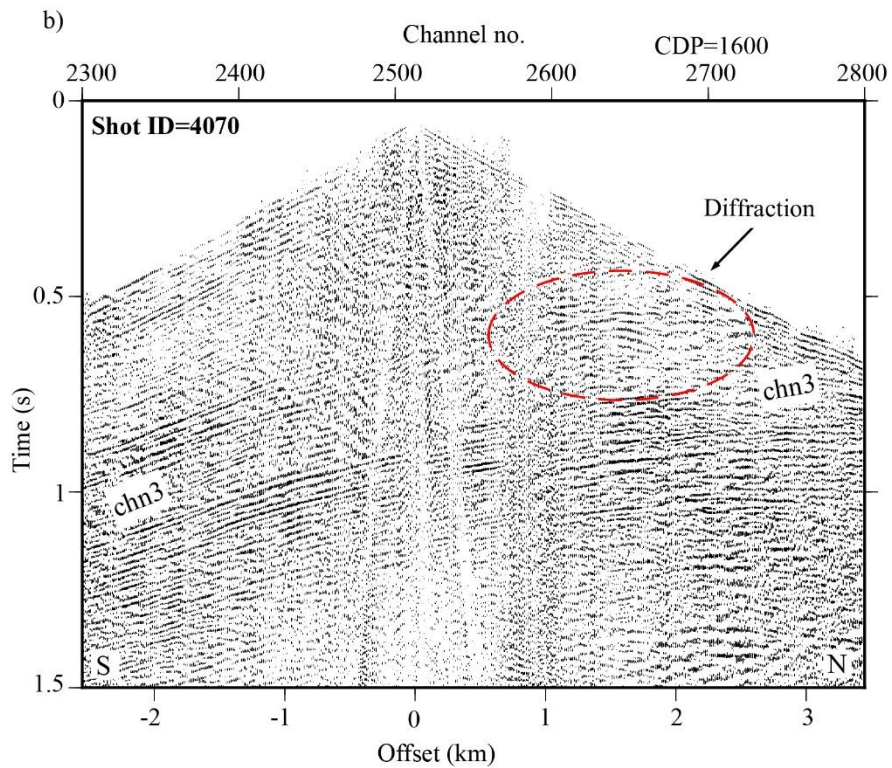
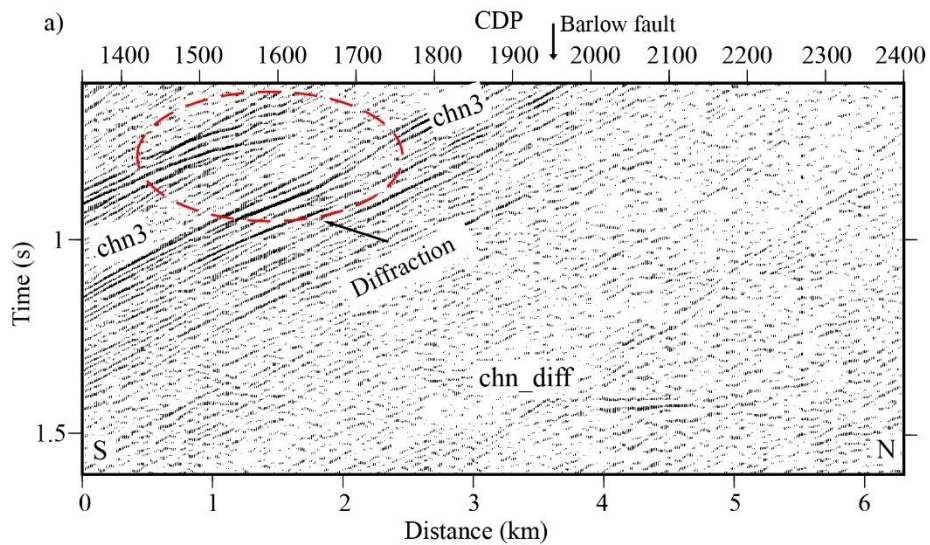
543

544

545

546

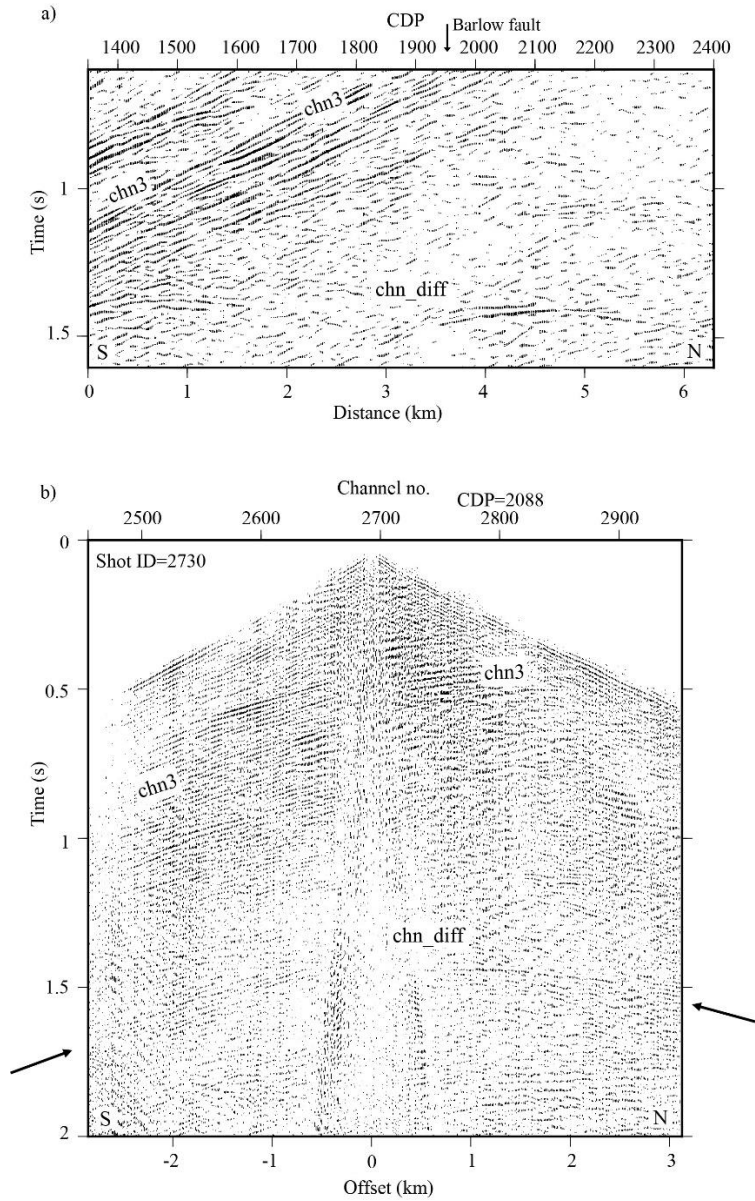
547



548
549
550
551
552

Figure 10: (a) A zoomed view from Fig. 8c (DMO stacked section with no cross-dip element applied) around the diffraction imaged. (b) Shot 4070 (see Fig. 4 for the location) acquired for the north survey which shows the signal from the diffraction around CDP 1600 in (a). The location of CDP 1600 is shown in (b). See text for interpretation.

553
554
555



556
557
558
559
560
561

Figure 11: (a) A zoomed view from Fig. 8b (DMO stacked section with cross-dip element 12° to west applied) around the diffraction *chn_diff*. (b) Shot 2730 (see Fig. 4 for the location) acquired for the north survey which shows the signal from the diffraction *chn_diff*; the apex of *chn_diff* is imaged around CDP 2088 in (a). The location of CDP 2088 is shown in (b). See text for interpretation.

562 Reflection sequence chs2 (Fig. 6, Table 3) also correlates with the contact between the Obatogamau (sedimentary rock) and
563 Caopatina Formations (mafic rocks), but includes two packages of reflectivity including a set of steeply dipping reflections
564 and another set of subhorizontal reflections (Fig. 6). The surface geology associated with the subhorizontal set of chs2 contains
565 mafic rocks of the Obatogamau Formation. The surface location of the Guercheville fault is marked at CDP 2400, thus the
566 reflection set of chs2 could be associated with this fault. The Guercheville fault is described as subvertical (Daigneault, 1996).
567 The reflection chs2 has a 40° dip to south in the migrated section (Fig. 6 and Table 3), which is much less than the reported
568 field measurements. Further knowledge about the geometry of reflection chs2, if associated with the Guercheville fault, would
569 help to better understand the subsurface architecture and its relationship to gold deposits along strike to the east.

570
571 CDMO analysis along the south survey (Fig. 9) suggested dips for reflection chs2 varying between 20°-50° depending on
572 different CDMO correction values. To evaluate CDMO results around chs2 shot gather 15135 is considered. Figure 12 shows
573 shot gather 15135 from the south survey (see Fig. 4d for location) that was acquired near CDP 2220 where chs2 turns from a
574 steeply-dipping reflector into a subhorizontal reflector (see Figs. 6 and 9). The chs2 reflection in this shot gather shows both
575 subhorizontal and steeply-dipping parts at approximately 1 s (see the dashed line in Fig. 12, which separates those parts). The
576 steeply dipping part of chs2 in Fig. 12 has an associated high apparent velocity (~8000 m/s), required so that a reflector dipping
577 ~ 40°-50° constructively stacks; this appears consistent with Fig. 9c (no cross-dip applied) and sections with cross-dip element
578 to east (Fig. 9d, 9e, and 9f). These reflections are also imaged with westward CDMO (Fig. 9a and 9b). This uncertainty would
579 suggest greater complexity of the Guercheville fault off the plane of the south profile. The angle between the southern profile
580 and the strike of the Guercheville fault where the profile crosses the fault is ~ 40°. This means that the true dip of the fault is
581 higher than the apparent dips imaged with reflection chs2 in Fig. 9, i.e., greater than 50°. Both scenarios including the cross-
582 dip element to east or west could therefore be valid. It appears that the structure associated with the reflection chs2, the
583 Guercheville fault, is a steeply dipping structure and shows an asymmetric anticline structure with its eastern flank steeper
584 than its western flank, i.e., the cross-dip of 40° to east in Fig. 9f vs. 12° to west in Fig. 9b. Using either cross-dip coherently
585 images reflection chs2 with an apparent dip of 50° along the profile.

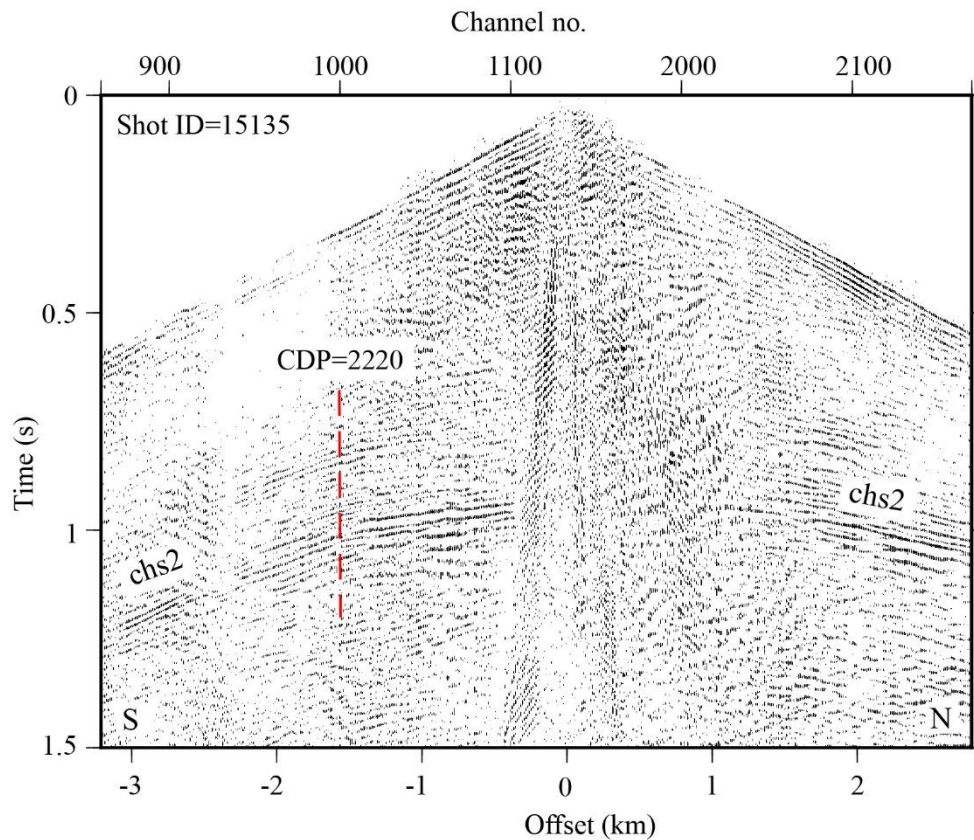
586
587 Similar to reflection sets chs1 and chs2, the reflection set chs3 (Fig. 6, Table 3) correlates with the contact between the
588 Obatogamau and Caopatina Formation at CDP 500. Unlike the reflection sets chs1 and chs2, the chs3 set dips to the north
589 (30°, Table 3) and represents the deepest reflector associated with the contact of the Obatogamau and Caopatina formations
590 along the south survey (Table 3). The CDMO analysis implies that the north dipping reflector chs3 shows more coherency
591 with westward strike (12°-30°, Fig. 9b and 9a, respectively). The reflector chs3 is less coherent at depths shallower than 2 km.
592 This may suggest a steeper dip that CDMO was not able to image.

593
594 Reflection chs4 (Fig. 6, Table 3), located at depths of 2-5 km, dips towards the north with a westward cross-dip element.
595 Because the seismic profile lies oblique to the strike of the mapped geological structures (Fig. 1), the true dip of this reflection

596 is greater than 30° (Table 3). Reflection chs4 likely images structures off the seismic profile in the south (Fig.1). This reflection
597 set probably lies within mafic rocks of the Obatogamau or Waconichi formations; therefore, it most likely originates at more
598 felsic interlayers, chert and iron formations, sulphide (VMS) accumulations, or faults within the mafic rocks. Reflection chs4
599 could alternatively be associated with structures from the northern border of the Lac Surprise Pluton (Fig. 1). If interpreted as
600 a fault, reflection chs4 most likely correlates to the Doda fault. The Doda fault is measured as subvertical at surface
601 (Daigneault, 1996). Reflection chs4 may image the extension of this fault at depths greater than 2 km.

602
603 At depths of 6-9 km, two packages of dipping reflections, chs5 to north and chs6 to south (Fig. 6, Table 3), suggest a syncline
604 structure. These reflectors may correspond to the proposed basal contact of greenstones with underlying tonalite-trondhjemite-
605 granodiorite (TTG) or tonalite-trondhjemite-diorite (TTD) intrusive rocks (Mathieu et al., 2020a). Alternatively, the reflectors
606 may lie within these intrusive rocks as represented by outcrops of the Hébert pluton to the south of the profile (Mathieu et al.,
607 2020b). At shallower depths, reflection sets chs3 and chs4 (north dipping, Fig. 6, and Table 3) and chs2 (south dipping, Fig.
608 6, Table 3) appear consistent with a regional syncline, perhaps the Druillettes syncline (Mathieu et al., 2020a).

609
610
611
612
613
614
615
616
617
618
619
620
621
622
623
624



625
626
627
628
629
630

Figure 12: Shot gather 15135 acquired for the south survey (see Fig. 4 for the location). A package of reflections interpreted as chs2 in Fig. 6 is imaged in this shot; The location of CDP 2220 is marked (see Figs. 6 and 9 for the location) and is marked on the shot. This CDP location shows separation of subhorizontal and steeply-dipping part of chs2. See text for interpretation.

631 6.3 Potential for exploration of orogenic gold

632

633 The Barlow fault and the associated diffractions in the north (reflection package chn3, Fig. 5) and in the south, the joint
634 compound structure of the Guercheville fault (reflection package chs2, Fig. 6) and the Doda fault (reflection package chs4,
635 Fig. 6) all lie within the greenstone belt rocks of the upper crust (Mathieu et al., 2020a). Both surveys show deep reflectors,
636 reflections chn5 and chn6 along the north profile and reflections chs5 and chs6 along the south profile, that appear related to
637 regional synclines. Fault zones within Abitibi greenstone rocks are recognized to host the orogenic gold deposits, for example,
638 the Cadillac-Larder Lake Fault Zone (Robert et al., 2005). One major attribute of the orogenic gold systems is their association
639 with steeply dipping (at least in the upper crust) crustal-scale faults (e.g. Cadillac-Larder Lake fault). Although the faults in

640 the Chibougamau area discussed here are mapped regionally over tens of kilometers (Fig. 1), at depth they dip shallowly (e.g.,
641 chn3 in Fig. 5) and do not extend deep within the crust. Thus, these are not faults typically thought to promote Au
642 mineralization. Bedeaux et al. (2020) inclusively studied the kinematic and metamorphism of the Barlow fault zone in
643 comparison with the Cadillac-Larder Lake Fault Zone. They explained that an absence of second-order structures connected
644 to the Barlow fault and an insufficient thickness of deep marine sedimentary rocks prevents ponding of deep metamorphic
645 fluids necessary to produce orogenic gold deposits. Few gold deposits are reported in the Barlow fault zone area (Lafrance,
646 2018). Nevertheless, the three faults imaged and discussed here and the diffractions imaged around the Barlow fault zone could
647 potentially be targeted for more detailed exploration as representing small orebody lenses.
648 .

649 **7 Conclusions**

650 Analysis of high-resolution seismic profiles in the Chibougamau area revealed the crucial role of survey geometry on seismic
651 illumination. Seismic data processing steps such as DMO corrections and PSTM proved to be highly dependent on a regular
652 offset distribution of CMPs in CDP bins for their effectiveness and further dependent on an optimized offset range that provides
653 better illumination in the presence of a complex subsurface architecture. The regular distribution of CMPs directly affects the
654 performance of DMO and PSTM algorithms. A detailed velocity model also increases the seismic illumination and improves
655 the performance when a DMO or PSTM algorithm is utilized. The key step in our study for optimized DMO and PSTM
656 processing is the investigation of offset distribution in order to choose an offset range in which most of the CDP bins show
657 regular distribution and thus contribute better to each process. We specifically investigated this for two high-resolution seismic
658 surveys with offsets in a range of 0-9 km and the analysis indicated that an offset range of 0-3 km provides more regular
659 sampling. Further investigation performed on the common-offset DMO correction process and common-offset PSTM for the
660 entire available offset range of 0-9 km (at a step rate of 3 km) indicated that both profiles showed their best results for the
661 offset range of 0-3 km. This offset range, along with a detailed velocity model, also provides the better illumination for DMO
662 and PSTM.

663
664 The subsurface architecture in the Chibougamau area has complex structure within its fault systems, these fault systems
665 potentially correspond to metal (gold) endowment and thus provide a major motivation for the survey and the processing trials.
666 The comprehensive processing work flow applied in this study improved the imaging of several major faults in the area. The
667 crooked nature of the surveys encouraged performing CDMO analysis to take into account the effect of out-of-plane structures.
668 The seismic imaging revealed the general trend of south dipping structures including the Barlow fault along the north survey
669 to depths of 5 km. The CDMO-DMO stacked sections imaged some diffractions along the north profile within the reflection
670 package associated with the Barlow fault. The seismic image also shows the thickening of the supracrustal sequence of rocks
671 beneath the Barlow fault within the regional Wachonachi syncline. The seismic imaging along the south profile implies a

672 moderate thickening of the supracrustal sequence and metasedimentary rocks between reflections associated with the
673 Guercheville and Doda faults in the form of a regional synform. The Guercheville fault relates to south dipping reflectors on
674 the north limb of the mapped regional Druillettes syncline and numerous gold showings along its strike. The DMO-CDMO
675 results indicate a local anticlinal fault geometry. The south profile did not cross the Doda fault directly, but did image several
676 structures which project upward to known faults and lithological contacts in the southern Chibougamau area. This work
677 contributes important constraints on the geometry and depth extent of these structures. The seismic imaging implies that the
678 Doda fault forms a steeply north-dipping reflector at depths greater than 2 km.

679 **8 Appendix A: evaluating survey geometry for DMO and PSTM**

680 For a 3D survey, equal azimuthal distribution, typically contributed by inline and crossline components, satisfies the symmetric
681 sampling (Vermeer 1990, 1998 and 2010). In the case of a 2D survey, reciprocity of shot/receiver gathers suggest that
682 properties of the continuous wavefield in a common shot/VP gather are the same as the properties of a common receiver gather.
683 Sampling requirements are the same for both domains and results in symmetric sampling. The immediate requirement of the
684 2D symmetric sampling is that the continuous wave field should be alias-free for ground-roll and low velocity noise (Vermeer,
685 2010). To satisfy an alias-free, continuous wavefield sampling, the basic sampling interval (Δx) is defined as Eq. (A1)
686 (Vermeer, 2010):

$$687 \Delta x = \frac{V_{min}}{2f_{max}} \quad (A1)$$

688 where V_{min} is the minimum apparent velocity and f_{max} is the maximum frequency of data. The VP and receiver spacing for
689 high-resolution surveys in the Chibougamau area are 6.25 m and 12.5 m, respectively (Table 1). For a representative shot
690 gather (receiver spacing of 12.5 m) and an estimated maximum frequency range of 60-120 Hz, the minimum apparent velocity
691 would be 1500-3000 ms⁻¹, and for a receiver gather with shot spacing of 6.25 m the minimum apparent velocity would be 750-
692 1500 ms⁻¹. These calculated apparent velocities indicate that the Chibougamau profiles are alias-free regarding shear waves
693 and ground roll.

694
695 The basic signal sampling interval (d) required to acquire a desired part of the continuous wavefield, (i.e., P- wave energy)
696 alias-free can be defined with Eq. (A1) and V_{min} is the minimum apparent velocity in the signal part, e.g., 5000-5500 ms⁻¹ for
697 a typical crystalline rock environment. Assuming these velocities, the receiver and VP spacing in Chibougamau profiles are
698 much smaller than the basic requirement and the acquired signal is alias-free for P-wave energy. The benefit of acquiring alias-
699 free signal for receiver /VP gathers is that those gathers act as an anti-alias filter for remaining low velocity noise (e.g., 300-
700 1500 ms⁻¹ in Chibougamau profiles).

701

702 Acquiring a seismic survey on the planned shot and receiver locations is not always practical due to natural obstacles or
 703 economic considerations. Gaps result in missed shots/receivers and sparse CMP distribution for some locations, or acquiring
 704 extra shots in other places with a resulting coarse CMP coverage. The crooked geometry exacerbates the effect of improper
 705 CMP distribution. The irregularity of a survey is defined as sparse CMP distribution in some parts of the survey and
 706 overabundance of CMPs in other parts (Beasley and Klotz, 1992). Some of the essential multichannel processing steps, and
 707 especially wave equation processes such as Kirchhoff PSTM and/or DMO corrections, assume that shots and receivers were
 708 acquired in nominal places and that a continuous CMP coverage (regular geometry) was fulfilled. The irregular geometry may
 709 lead to artefacts or footprints for PSTM and DMO process (Canning and Gardner, 1998; Schuster and Liu, 2001). The effects
 710 of those artefacts on Kirchhoff PSTM algorithms and DMO corrections can be defined basically as a concept of an integral
 711 summation (Canning and Gardner, 1998):

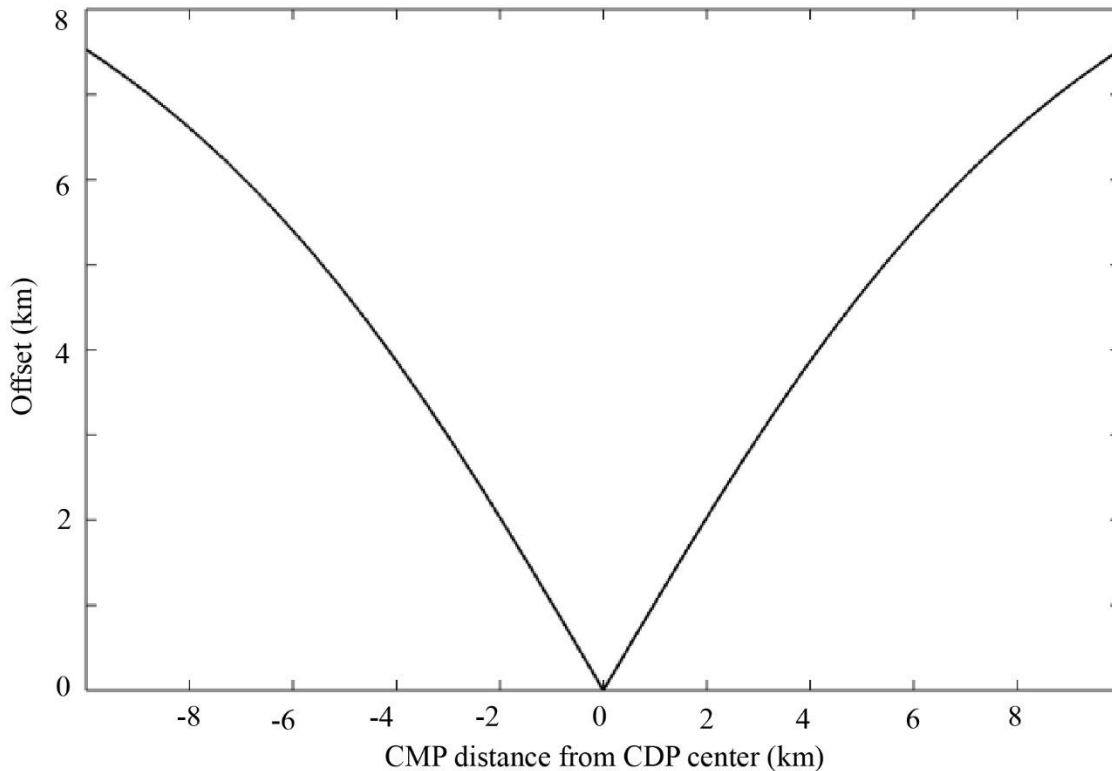
$$712 \quad f(x, y, z) = \int w \frac{d}{dt} f(S, R, \tau) dSdR \quad (A2)$$

713 S and R represents shot and receiver coordinates, respectively; (x, y, z) is a diffraction point (p) and τ is traveltime along the
 714 diffraction surface generated by (p). When common-offset gathers are considered for PSTM algorithms or DMO corrections,
 715 $dSdR$ will be the CMP coordinate, i.e. $dx_m dy_m$ where x_m and y_m are CMP coordinates and offset planes are shown by w .
 716 For a regular geometry offset increments are constant and thus we can assume that $dx_m dy_m$ is constant and offset planes (w)
 717 including short and long offsets contribute equally in the Eq. (A2). In a case of irregular geometry, CMP locations (i.e.
 718 $dx_m dy_m$) and w (i.e. offset planes) will contribute irregularly in the Eq. (A2). For a Kirchhoff style PSTM if CMPs are
 719 irregularly distributed (per their offsets), the migrated traces would destructively contribute in the stacking process and the
 720 resulting seismic image will be blurred (Yilmaz, 2001). For DMO corrections, an imaging point represents a contribution of
 721 CMPs for both short and long offsets in the DMO formula (Deregowski, 1982). If some of the offsets are missing around the
 722 imaging point, the DMO process generates artefacts (Vermeer, 2012), generally in the form of subhorizontal features that
 723 disguise the seismic image (Cheraghi et al., 2012).

724
 725 To further investigate the effect of regular offset plane for DMO corrections, we generated an example of common-offset
 726 DMO corrections which is shown in Fig. A1 based on the seismic wave velocities typically observed in crystalline rock
 727 environments. The graph has been provided from DMO formula (Hale, 1991) with considering common-offset method
 728 (Fowler, 1998). This graph implies that the missing offsets (i.e., irregularity) hinder the DMO correction process, i.e., the curve
 729 will be discrete.

730
 731 The above mentioned irregularity of the wave equation processes and its effect has been subject of many studies (e.g., Williams
 732 and Marcoux, 1989; Ronen, et al., 1995;). The less studied subject is CMP contribution into subsurface illumination of those
 733 processes (e.g., DMO fold, Vermeer, 1994; Ferber, 1997). The conventional CMP stacking fold is defined based on total
 734 number of traces sharing a reflector point on a flat surface. All these traces contribute to the subsurface illumination (Beasley

735 and Klotz, 1992; Beasley, 1993; Ferber, 1997). The standard CMP stacking can also be applied to single-dip reflectors, if dip-
736 dependent velocity (i.e., apparent velocity), is considered (Jakubowicz, 1990). Cases of lateral velocity changes, diffractions,
737 and conflicting dips require more advanced processes. Pre-stack depth migration provides an efficient solution for apparent
738 velocity cases whereas the other cases need DMO or PSTM to be applied (Jakubowicz, 1990). For a particular reflector with
739 an arbitrary dip and strike the DMO fold (or DMO illumination) is considered to be those traces that contribute to the process
740 constructively (Ferber, 1997). For a given source and receiver location, constructive DMO illumination takes place if the
741 difference between DMO and NMO corrected travel-time reflection and zero-offset travel-time reflector is less than half of
742 the dominant wavelength (Ferber, 1997). In the best case scenario, DMO fold is equal to CMP stacking fold (Vermeer, 2010).
743 The DMO illumination can be investigated during survey design with numerical modeling of seismic response where different
744 scenarios are considered for subsurface architecture (Beasley, 1993). For the acquired geometry, the regularity of CMPs is the
745 most crucial factor which defines the optimized performance of any wave equation process (DMO and PSTM, Canning and
746 Gardner, 1998).
747



748
749 **Figure A1:** The regular offset distribution in a CDP bin for DMO corrections calculated from DMO formula (see Hale, 1991; Fowler, 1998).
750 The offset range is considered 0-8 km; the average velocity is considered 5500 ms^{-1} to be representative of crystalline rocks. The recording
751 length is 4 s with sampling rate of 2 ms (similar to Chibougamau high-resolution seismic surveys, see Table1). Target depth is located at 1s.

752 **9 Data availability**

753 The data that support the findings of this study are available from Metal Earth project. Restrictions apply to the availability of
754 these data, which were used under license for this study. Data are available from the authors with the permission of Metal
755 Earth project. For more information, please visit Metal Earth webpage at <https://merc.laurentian.ca/research/metal-earth>.

756 **10 Author contribution**

757 SCH processed seismic data and prepared the methodology and wrote the original draft and constructed all the figures. AM
758 contributed to seismic data processing and writing the original draft. SCH, AM, MN, DS, LM, and PB contributed to
759 interpretation, writing and editing. DS designed the seismic survey.

760 **11 Competing interests**

761 The authors declare that they have no conflict of interests.

762 **12 Acknowledgments**

763 This research was funded by the NSERC Canada First Research Excellence Fund. The authors would like to thank the Metal
764 Earth project at Laurentian University for providing and archiving the seismic data. S. Cheraghi acknowledges Metal Earth
765 for funding his research. Globe Claritas was used for seismic processing. GMT from P. Wessel and W.H.F. Smith was used to
766 prepare some of the figures. GOCAD was used for 3D visualization and interpretation. The authors would like to thank Kipp
767 Grose for IT support during processing of Metal Earth seismic surveys. Dean Meek is acknowledged to have provided
768 geological and geographical maps in the study area. The authors would like to appreciate frontline and essential workers who
769 risk their lives during pandemic spread of the COVID-19. This is a collaboration of Metal Earth and Smart Exploration. Smart
770 Exploration has received funding from the European Union's Horizon 2020 research and innovation program under grant.
771 This is Metal Earth publication MERC-ME-2020-093.

772

773

774

775

776

777 **13 References**

- 778 Adam, E., Milkereit, B., and Mareschal, M.: Seismic reflection and borehole geophysical investigations in the Matagami
779 mining camp, Canadian Journal of Earth Sciences, 35, 686–695, 1998.
- 780 Adam, E., Perron, G., Milkereit, B., Wu, J., Calvert, A.J., Salisbury, M., Verpaelst, P., and Dion, D.J.: A review of high-
781 resolution seismic profiling across the Sudbury, Selbaie, Noranda, and Matagami mining camps, Canadian Journal of Earth
782 Sciences, 37, 503–516, 2000.
- 783 Adam, E., Perron, G., Arnold, G., Matthews, L., and Milkeriet, B.: 3D seismic imaging for VMS deposit exploration,
784 Matagami, Quebec, in: Hardrock seismic exploration, edited by: D.W. Eaton, B. Milkereit, and M.H. Salisbury, SEG, 229–246,
785 2003.
- 786 Ahmadi, O., Juhlin, C., Malehmir, A., and Munck, M.: High-resolution 2D seismic imaging and forward modeling of a
787 polymetallic sulfide deposit at Garpenberg, central Sweden, Geophysics, 78, no. 6, B339–B350, 2013.
- 788 Beasley, C.J.: Quality Assurance of Spatial Sampling: SEG, Washington, 544–547, 1993.
- 789 Beasley, C.J., and Klotz, R.: Equalization of DMO for Irregular Spatial Sampling, SEG, New Orleans, 970–973, 1992.
- 790 Bedeaux, P., Brochu, A., Mathieu, L., Gaboury, D., Daigneault, R.: Structural analysis and metamorphism of the Barlow Fault
791 Zone, Chibougamau area, Neoproterozoic Abitibi Subprovince: Implications for gold mineralization, Canadian Journal of earth
792 Sciences, accepted, 2020.
- 793 Bellefleur, G., Barnes, A., Calvert, A.J., Hubert, C., and M. Mareschal, 1995: Seismic reflection constraints from Lithoprobe
794 line 29 on the upper crustal structures of the northern Abitibi greenstone belt, Canadian Journal of Earth Sciences, 32, 128–
795 13, 1995.
- 796 Bellefleur, G., Calvert, A.J., and Chouteau, M.C.: Crustal geometry of the Abitibi Subprovince, in light of three-dimensional
797 seismic reflector orientation, Canadian Journal of Earth Sciences, 35, 569–582, 1998.
- 798 Bellefleur, G., Schetselaar, E., White, D., Miah, K., and Dueck, P.: 3D seismic imaging of the Lalor volcanogenic massive
799 sulphide deposit, Manitoba, Canada, Geophysical Prospecting, 63, no. 4, 813–832, 2015.
- 800 Bellefleur, G., Cheraghi, S., and Malehmir, A.: Reprocessing legacy 3D seismic data from the Halfmile Lake and Brunswick
801 No. 6 VMS deposits, New Brunswick, Canada, Canadian Journal of Earth Sciences, 56(5), 569–583, 2019.
- 802 Bédard, J. H., Leclerc, F., Harris, L.B., and Goulet, N.: Intra-sill magmatic evolution in the Cummings Complex, Abitibi
803 greenstone belt: Tholeiitic to calc-alkaline magmatism recorded in an Archaean subvolcanic conduit system, Lithos, 111, no.
804 1, 47–71, 2009.
- 805 Braunig, L., Buske, S., Malehmir, A., Backstrom, E., Schon, M., and Marsden, P.: Seismic depth imaging of iron-oxide
806 deposits and their host rocks in the Ludvika mining area of central Sweden, Geophysical Prospecting, 68, 24–43, 2020.
- 807 Canning, A., and Gardner, G.H.F.: Reducing 3D acquisition footprint for 3D DMO and 3D prestack migration, Geophysics,
808 63, no. 4, 1177–1183, 1998.

809 Cheraghi, S., Malehmir, A., and Bellefleur, G.: Crustal-scale reflection seismic investigations in the Bathurst Mining Camp,
810 New Brunswick, Canada, *tectonophysics*, 506 (1–4), 55–72, 2011.

811 Cheraghi, S., Malehmir, A., and Bellefleur, G.: 3D imaging challenges in steeply dipping mining structures: new lights on
812 acquisition geometry and processing from the Brunswick No. 6 seismic data, Canada, *Geophysics*, 77, no. 5, WC109–WC122,
813 2012.

814 Cheraghi, S., Malehmir, A., Bellefleur, G., Bongajum, E., and Bastani, M.: Scaling behavior and the effects of heterogeneity
815 on shallow seismic imaging of mineral deposits: A case study from Brunswick No. 6 mining area, Canada, *Journal of Applied*
816 *Geophysics*, 90, 1–18, 2013.

817 Cheraghi, S., Naghizadeh, M., Snyder, D.B., and Mathieu, L.: Crustal-scale seismic investigation in Chibougamau, Quebec,
818 Canada, 2nd Conference on Geophysics for Mineral Exploration and Mining, Workshop: worldwide Mineral Exploration
819 Challenges and Cost-effective Geophysical Methods, EAGE, Porto, Portugal, 2018.

820 Deregowski, S.M.: Dip-moveout and reflector point dispersal, *Geophysical Prospecting*, 30, 318–322, 1982.

821 Daigneault, R., St-Julien, P., and Allard, G.O.: Tectonic evolution of the northeast portion of the Archean Abitibi greenstone
822 belt, Chibougamau area, Quebec, *Canadian Journal of Earth Sciences*, 27(12), 1714–1736, 1990.

823 Daigneault, R. : Couloirs de déformation de la Sous-province de l’Abitibi, Ministère des Ressources Naturelles du Québec, MB
824 96–03. 140 pages. 1996.

825 David, J., Vaillancourt, D., Bandyayera, D., Simard, M., Goutier, J., Pilote, P., et al.: Datations U- Pb Effectuées dans les
826 Sous-provinces d’Ashuanipi, de La Grande, d’Opinaca et d’Abitibi en 2008- 2009. MERN report, RP- 2010- 11; Ministère de
827 l’Énergie et des Ressources Naturelles: Québec, QC, Canada, 2011.

828 Dimroth, E., Rochelau, M., Mueller, W., Archer, P., Brisson, H., Fortin, G., Jutras, M., Lefebvre, C., Piche, M., Pilote, P., and
829 Simoneau, P.: Paleogeographic and paleotectonic response to magmatic processes – a case-history from the Archean sequence
830 in the Chibougamau area, Quebec, *Geologische Rundschau*, 74, 11–32, 1985.

831 Dimroth, E., Mueller, W., Daigneault, R., Brisson, H., Poitras, A., and Rocheleau, M.: Diapirism during regional compression:
832 the structural pattern in the Chibougamau region of the Archean Abitibi Belt, Quebec, *Geologische Rundschau*, 75(3), 715–
833 736, 1986.

834 Ferber, R.: What is DMO coverage, 59th Annual International Meeting, EAGE, Geneva, Switzerland, A049, 1997.

835 Fowler, P.J.: A comparative overview of prestack time migration methods, 67th Annual International meeting, SEG,
836 1571–1574, 1997.

837 Fowler, P.J.: A comparative overview of dip moveout methods, Annual Meeting, SEG, 1744, 1998.

838 Groves, D.I., Goldfarb, R.J., Gebre-Mariam, M., Hagemann, S.G., and Robert, F.: Orogenic gold deposits—a proposed
839 classification in the context of their crustal distribution and relationship to other gold deposit types, *Ore Geology Reviews*, 13,
840 7–27, 1998.

841 Hale, D.: A nonaliased integral method for dip moveout: *Geophysics*, 56, no. 6, 795–805, 1991.

842 Heinonen, S., Malinowski, M., Hloušek, F., Gislason, G., Buske, S., Koivisto, E. and Wojdyla, M.: Cost-effective seismic
843 exploration: 2D reflection imaging at the Kylylahti massive sulfide deposit, Finland, *Minerals*, 9, no. 5, 263, 2019.

844 Jakubowicz, H.: A simple efficient method of dip-moveout correction, *Geophysical Prospecting*, 38, 221–245, 1990.

845 Juhlin, C.: Imaging of fracture zones in the Finnsjön area, central Sweden, using the seismic reflection method, *Geophysics*,
846 60, 66–75, 1995.

847 Juhlin, C., Kashubin, A.S., Knapp, J., Makovsky, V., and Ryberg, T.: EUROPROBE seismic reflection profiling in the Urals:
848 The ESRU project, *EOS*, 76, 193–198, 1995.

849 Juhlin, C., Dehghannejad, M., Lund, B., Malehmir, A., and Pratt, G.: Reflection seismic imaging of the end-glacial Pärvie
850 Fault system, northern Sweden, *Applied Geophysics*, 70, no. 4, 307–316, 2010.

851 Kashubin, A.S., and Juhlin, C.: Mapping of crustal scale tectonic boundaries in the Ossa-Morena Zone using reprocessed
852 IBERSEIS reflection seismic data, *Tectonophysics*, 489, 139–158, 2010.

853 Lafrance, B.: Travaux d'exploration 2016-2017, Project Richardson, Chibougamau, Quebec, Tarku Resources, GM 70535,
854 132p, 2018

855 Lerner, K. L., Gibson, B. R., Chambers, R., and Wiggins, R. A.: Simultaneous estimation of residual static and crossdip
856 corrections: *Geophysics*, 44, 1175–1192, 1979.

857 Leclerc, F., Harris, L.B., Bedard, J.H., van Breemen, O., and Goulet, N.: Structural and stratigraphic controls on magmatic,
858 volcanogenic, and shear zone-hosted mineralization in the Chapais-Chibougamau mining camp, northeastern Abitibi, Canada,
859 *Economic Geology*, 107, no. 5, 963–989, 2012.

860 Leclerc, F., Roy, P., Houle, P., Pilote, P., Bedard, J.H., Harris, L.B., McNicoll, V., Van Breemen, O., David, J., and Goulet,
861 N.: Géologie de la région de Chibougamau, Ministère de l'Énergie et des Ressources Naturelles, RG 2015-03. 97 p, 2015.

862 Leclerc, F., Roy, P., Pilote, P., Bédard, J.H., Harris, L.B., McNicoll, V.J., et al. : Géologie de la Région de Chibougamau :
863 MERN report RG 2015-03, Ministère de l'Énergie et des Ressources Naturelles, Québec, QC, Canada, 2017.

864 Lundberg, E., and Juhlin, C.: High resolution reflection seismic imaging of the Ullared Deformation Zone, southern Sweden,
865 *Precambrian Research*, 190, 25–34, 2011.

866 Malehmir, A., and Bellefleur, G.: Reflection seismic imaging and physical properties of base-metal and associated iron
867 deposits in the Bathurst Mining Camp, New Brunswick, Canada, *Ore Geology Reviews*, 38, 319–333, 2010.

868 Malehmir, A., Bellefleur, G., and Müller, C.: 3D diffraction and mode converted scattering signatures of base-metal deposits,
869 Bathurst Mining Camp, Canada, *First Break*, 28, 41–45, 2010.

870 Malehmir, A., Dahlin, P., Lundberg, E., Juhlin, C., Sjöström, H., and Högdahl, K.: Reflection seismic investigations in the
871 Dannemora area, central Sweden: Insights into the geometry of polyphase deformation zones and magnetite- skarn deposits,
872 *Journal of Geophysical Research*, 116, B11307, 2011.

873 Malehmir, A., Durrheim, R., Bellefleur, G., Urosevic, M., Juhlin, C., White, D., Milkeriet, B., and Campell, G.: Seismic
874 methods in mineral exploration and mine planning: A general overview of past and present case histories and a look into the
875 future, *Geophysics*, 77, no. 5, WC173– WC190, 2012.

876 Mathieu, L., and Racicot, D.: Petrogenetic Study of the Multiphase Chibougamau Pluton: Archean Magmas Associated with
877 Cu-Au Magmato-Hydrothermal Systems, *Minerals*, 9, no. 3, 174, 2019.

878 Mathieu, L., Crépon, A., and Kontak, D.J.: Tonalite-dominated magmatism in the Abitibi Subprovince, Canada, and
879 significance for Cu-Au magmatic-hydrothermal systems, *Minerals*, 10, 242, 2020a.

880 Mathieu, L., Snyder, D.B., Bedeaux, P., Cheraghi, S., Lafrance, B., Thurston, P., and Sherlock, R.: Deep into the Chibougamau
881 area, Abitibi Subprovince: structure of a Neoproterozoic crust revealed by seismic reflection profiling, *Tectonics*, 38, 1–25, 2020b.

882 Mercier-Langevin, P., Lafrance, B., Bécu, V., Dubé, B., Kjarsgaard, I., and Guha, J. : The Lemoine auriferous volcanogenic
883 massive sulfide deposit, Chibougamau camp, Abitibi greenstone belt, Quebec, Canada : Geology and genesis, *Economic
884 Geology*, 109(1), 231–269, 2014.

885 Milkereit, B., and Eaton, D.: Imaging and interpreting the shallow crust, *Tectonophysics*, 286, 5–18, 1998.

886 Mueller, W., Chown, E.H., Sharma, K.N.M., Tait, L., and Rocheleau, M.: Paleogeographic and paleotectonic evolution of a
887 basement-controlled Archean supracrustal sequence, Chibougamau-Caopatina, Quebec, *The Journal of Geology*, 97, no. 4,
888 399–420, 1989.

889 Naghizadeh, M., Snyder, D.B., Cheraghi, S., Foster, S., Cilensek, S., Feloreani, E., and Mackie, J.: Acquisition and Processing
890 of Wider Bandwidth Seismic Data in Crystalline Crust: Progress with the Metal Earth Project, *Minerals*, 9 (145), 2019.

891 Nedimovic, M. R., and West, G. F.: Crooked- line 2D seismic reflection imaging in crystalline terrains: Part 1, data
892 processing, *Geophysics*, 68, 274–285, 2003.

893 Perron, G., Milkereit, B., Reed, L.E., Salisbury, M., Adam, E., and Wu, J.: Integrated seismic reflection and borehole
894 geophysical studies at Les Mines Selbaie, Quebec, *CIM Bulletin*, 90, 75–82, 1997

895 Perron, G., and Calvert, A.J.: Shallow, high-resolution seismic imaging at the Ansil mining camp in the Abitibi greenstone
896 belt, *Geophysics*, 63, no. 2, 379–391, 1998.

897 Pilote, P., Dion, C., Joannis, A., David, J., Machado, N., Kirkham, R.V., and Robert, F.: Géochronologie des minéralisations
898 d’affiliation magmatique de l’Abitibi, secteurs Chibougamau et de Troilus-Frotet: implications géotectoniques, in :
899 Programme et résumés, Séminaire d’information sur la recherche géologique (p. 47), MRN report, DV-97-03, Ministère des
900 Ressources Naturelles, Québec, QC, Canada, 1997.

901 Phillips, G.N., and Powell, R.: Formation of gold deposits: a metamorphic devolatilization model, *Journal of Metamorphic
902 Geology*, 28, no. 6, 689–718, 2010.

903 Robert, F., Poulsen, K.H., Cassidy, K.F., and Hodgson, C.J.: Gold metallogeny of the Superior and Yilgarn cratons, *Economic
904 Geology*, 100, 1001–1033, 2005.

905 Rodriguez- Tablante, J., Tryggvason, A., Malehmir, A., Juhlin, C., and Palm, H.: Cross- profile acquisition and cross- dip
906 analysis for extracting 3D information from 2D surveys, a case study from the western Skellefte District, northern Sweden,
907 *Journal of Applied Geophysics*, 63, 1–12, 2007.

908 Ronen, S., Nichols, D., Bale, R., Ferber, R.: Dealiasing DMO: Good-pass, bad-pass, and unconstrained, *SEG, Houston*, 743–
909 745, 1995.

910 Salisbury, M.H., Harvey, C.W., and Matthews, L.: The acoustic properties of ores and host rocks in hardrock terranes, in: Hard
911 rock seismic exploration, edited by: D.W. Eaton, B. Milkereit, and M.H. Salisbury, SEG, 9–19, 2003.

912 Sawyer, E.W., and Benn, K.: Structure of the high-grade Opatoca Belt and adjacent low-grade Abitibi Subprovince, Canada:
913 An Archaean mountain front, *Journal of Structural Geology*, 15(12), 1443–1458, 1993.

914 Schmelzbach, C., Juhlin, C., Carbonell, R., and Simancas, J.F.: Prestack and poststack migration of crooked-line seismic
915 reflection data: a case study from the South Portuguese Zone fold belt, southwestern Iberia, *Geophysics*, 72, no. 2, B9–B18,
916 2007.

917 Schuster, G.T., and Liu, Z.: Seismic array theorem and rapid calculation of acquisition footprint noise: *Geophysics*, 66, no. 6,
918 1843–1849, 2001.

919 Singh, B., Malinowski, M., Hlousek, F., Koivisto, E., Heinonen, S., Hellwig, O., Buske, S., Chamarczuk, M., and Juurela, S.:
920 Sparse 3D Seismic Imaging in the Kylylahti Mine Area, Eastern Finland: Comparison of Time Versus Depth Approach,
921 *Minerals*, 9, no. 5, 305, 2019.

922 Vermeer, G.J.O.: Seismic wavefield sampling, SEG, 1990.

923 Vermeer, G.J.O.: 3D symmetric sampling, 64th annual International Meeting, SEG, extended abstract, 906–909, 1994.

924 Vermeer, G.J.O.: 3D symmetric sampling, *Geophysics*, 63, no. 5, 1629–1647, 1998.

925 Vermeer, G.J.O.: 3D symmetric sampling of sparse acquisition geometries, *Geophysics*, 75, no. 6, WB3–WB14, 2010.

926 Vermeer, G.J.O.: 3D seismic survey design, second edition, SEG, 263–270, 2012.

927 Williams, R.G., and Marcoux, M.: Model-constrained anti-alias filtering for improved 3-D DMO, 51st Annual International
928 Meeting, EAGE, 1989.

929 Yilmaz, Ö.: Seismic data analysis, Processing, inversion, and interpretation of seismic data, SEG, 2001.

930